J. Fluid Mech. (2004), *vol.* 514, *pp.* 173–204.
DOI: 10.1017/S0022112004000163 Printed in the United Kingdom

Downstream evolution of the most energetic modes in a turbulent axisymmetric jet at high Reynolds number. Part 1. The near-field region

By DAEHAN JUNG[1], STEPHAN GAMARD[2] AND WILLIAM K. GEORGE[3]

[1]Department of Mechanical Engineering, Korean Air Force Academy, Cheongwon, Chungbuk 363-849, Korea

[2]Industrial Applications and Healthcare R & D, Praxair Inc., Tonawanda, NY 14150, USA

[3]Turbulence Research Laboratory, Department of Thermo and Fluid Dynamics, Chalmers University of Technology, Gothenburg, SE-41296, Sweden

(Received 29 May 2002 and in revised form 26 April 2004)

Experiments were carried out in an axisymmetric turbulent jet from 2 to 6 diameters downstream at exit Reynolds numbers of 78 400, 117 600, and 156 800. Data were collected using the 138 hot-wire probe constructed by Citriniti & George (2000). The proper orthogonal decomposition (POD) was then applied to a double Fourier transform in time and azimuthal direction of the two-point velocity correlation tensor. Azimuthal mode-0, which dominated the dynamics at $x/D = 3$ in the previous experiments, dies off rapidly downstream towards a non-zero value. For the higher azimuthal modes, the peak shifts from mode-6 towards lower azimuthal mode numbers with increasing downstream distance, until the peak is at mode-2 by the end of the potential core. The POD eigenspectra collapse in similarity variables for the mixing layer at all downstream positions, and are nearly independent of Reynolds number. Reconstruction of the full-field streamwise velocity component using the dominant POD modes shows clearly the evolution of the flow with downstream position, from 'volcano-type' eruptions at 2 to 3 diameters downstream to a 'propeller-like' pattern where the number of blades diminishes downstream.

1. Introduction

The existence of large-scale structures in turbulent flows has been recognized for a number of years. It has also long been suspected that these large-scale structures play important roles in many applications: chemical mixing, noise control, momentum transfer, drag reduction, combustion enhancement, etc. Since the large-scale structures are embedded inside the turbulent motions, it is very difficult to identify and extract them from the chaotic turbulent flows. The efforts over the past few decades, especially as applied to axisymmetric jets, have been the subject of many reviews (e.g. Cantwell 1981; Hussain 1983; Holmes, Lumley & Berkooz 1996; Citriniti & George 2000). The last of these used a proper orthogonal decomposition (POD) to extract the most energetic structures of the flow, and similar methodology will be used here and in Part 2 of this paper (Gamard, Jung & George 2004).

A particular advantage of the POD is that it leads directly to mathematical models. Its first application to the axisymmetric mixing layer without any controlled excitation showed that a low-dimensional description of the time-dependent velocity field was

possible (Leib, Glauser & George 1984). The much more extensive experiments of Glauser & George (1987) (see also Glauser 1987), who applied the POD to the radial direction of a jet mixing layer at 3 diameters downstream, showed that only the first few POD modes were necessary to capture most of the energy, with more than 40% in the first POD mode alone. That work described the azimuthal and temporal decomposition as well.

There have been a number of recent applications of the POD to turbulent free shear flows, all using rakes of probes to obtain the necessary cross-spectral data at a large number of locations. Ukeiley & Seiner (1998) and Ukeiley, Seiner & Ponton (1999) were the first to investigate the downstream evolution of the POD modes in the shear layer of an axisymmetric jet, similar to this study although at much higher Mach numbers. They showed that the behaviour of the eigenspectra changed drastically with downstream position. Taylor, Ukeiley & Glauser (2001) later applied linear stochastic estimation methods to the same database. Gordeyev & Thomas (2000) focused on the similarity region of a turbulent planar jet, while Delville *et al.* (1999) reported a thorough examination of the POD modes in a plane mixing layer. The second part of the latter study (Ukeiley *et al.* 2001) used the POD eigenfunctions to build low-order dynamical systems models to reconstruct the velocity field. The application of the POD to the near field of the jet prior to our study is reviewed in detail in Glauser *et al.* (2000).

In an abbreviated version of the experiment reported herein, Citriniti & George (2000) examined the dynamics of the jet mixing layer from instantaneous realizations of the streamwise velocity field at $x/D = 3$ using 138 simultaneously sampled hot-wire anemometer probes. The simultaneous measurements at many points allowed the POD eigenfunctions to be projected back onto a slice of the flow, so the instantaneous flow could be reconstructed as a whole, or in part, one piece at a time. These velocity reconstructions using the POD provided evidence for both azimuthally coherent 'volcano-like' events that contained most of the energy, and for counter-rotating, streamwise vortex pairs (or ribs) in the region between successive azimuthally coherent structures.

Both the Glauser and Citriniti experiments were performed at only a single downstream position and single Reynolds number. Our goal in this study is to investigate whether and how the modal character of the flow changed with downstream position and jet exit Reynolds number. In this experiment, data are presented at three Reynolds numbers, Re_D, of 78 400, 117 600, and 156 800 (based on jet exit velocity and diameter) at downstream positions ranging from $x/D = 2.0$ to 6.0 in increments of 0.5 diameters, all at low Mach numbers (< 0.07). This covers the spatial extent over which the mean velocity profile evolves from a top-hat to a nearly fully developed jet profile. Part 2 (Gamard *et al.* 2004) will present an extension of this work to the far-field region of the jet.

2. Experimental apparatus

2.1. *The axisymmetric jet*

The experiments were carried out in the turbulent mixing layer generated by an isothermal, non-reacting, incompressible, and axisymmetric jet. The jet was enclosed in a very large $4.3 \times 4.6 \times 11.4$ m^3 shield to minimize the effects of boundary conditions on the flow (Hussein, Capp & George 1994, Appendix B). This jet facility was used previously by Citriniti & George (2000) (as well as Glauser & George 1987) and has also been described thoroughly in Jung (2001). Air flow is generated from a

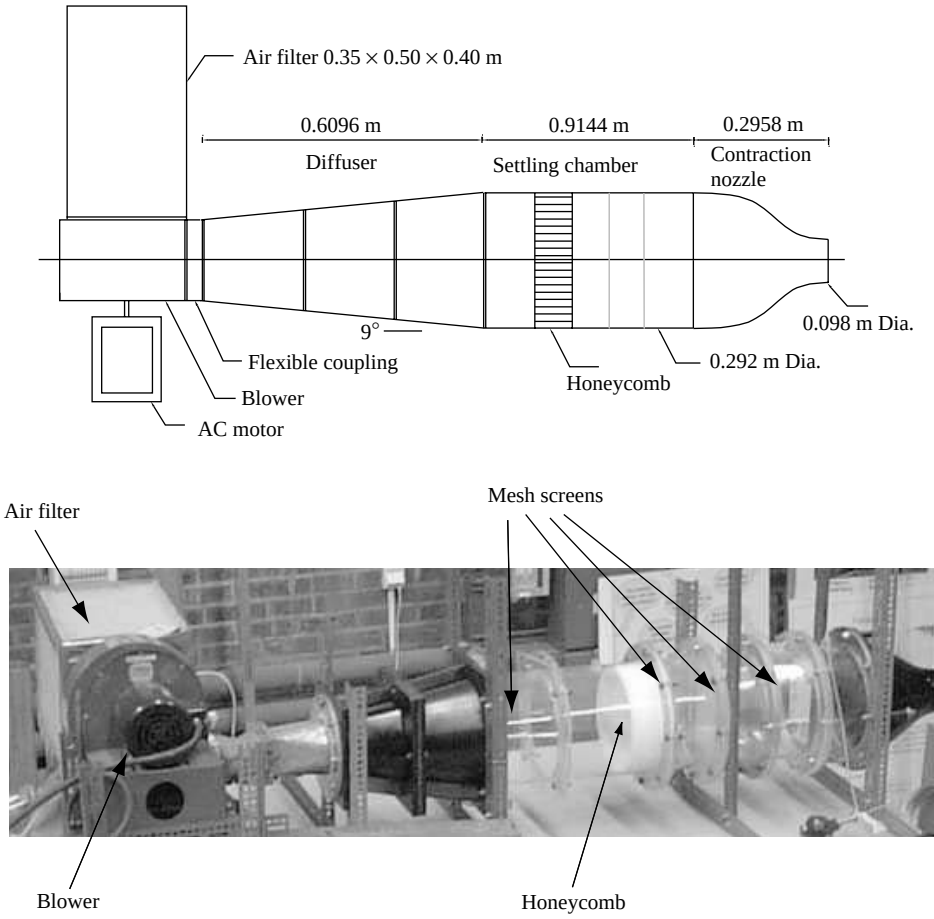

FIGURE 1. Schematic and photo of the jet facility.

blower-driven jet, figure 1, and exits through a fifth-order polynomial nozzle of 9.8 cm diameter. The turbulence intensity at the jet exit varied between 0.23% and 0.5%, depending on the jet velocity. The exit profile was a top-hat with a boundary layer of 1.2 mm based on δ_{99}.

2.2. *The probe array*

In order to be able to reconstruct the velocity from the POD eigenspectra, it is necessary to acquire all the signals simultaneously to avoid losing the phase information. For this purpose, Citriniti & George (2000) designed an array of hot wires with enough resolution to decompose the flow field at a fixed downstream position. Using the data of Glauser & George (1987) (or Glauser & George 1992) and the criteria for the azimuthal resolution necessary to avoid any azimuthal aliasing, Citriniti & George (2000) designed a probe array with 138 hot wires in six concentric circles, see figure 2. Using data from this probe array, the POD can resolve up to six eigenspectra in the radial direction, and up to 16 azimuthal modes.

An array of hot wires will still leave some unresolved scales that will be aliased into the measured signal. To avoid this, Citriniti & George (2000) used very long wires (1 cm long) oriented in the azimuthal direction to act as spatial filters. Since the signals from the turbulent flow are filtered out by the long sensing hot wire before

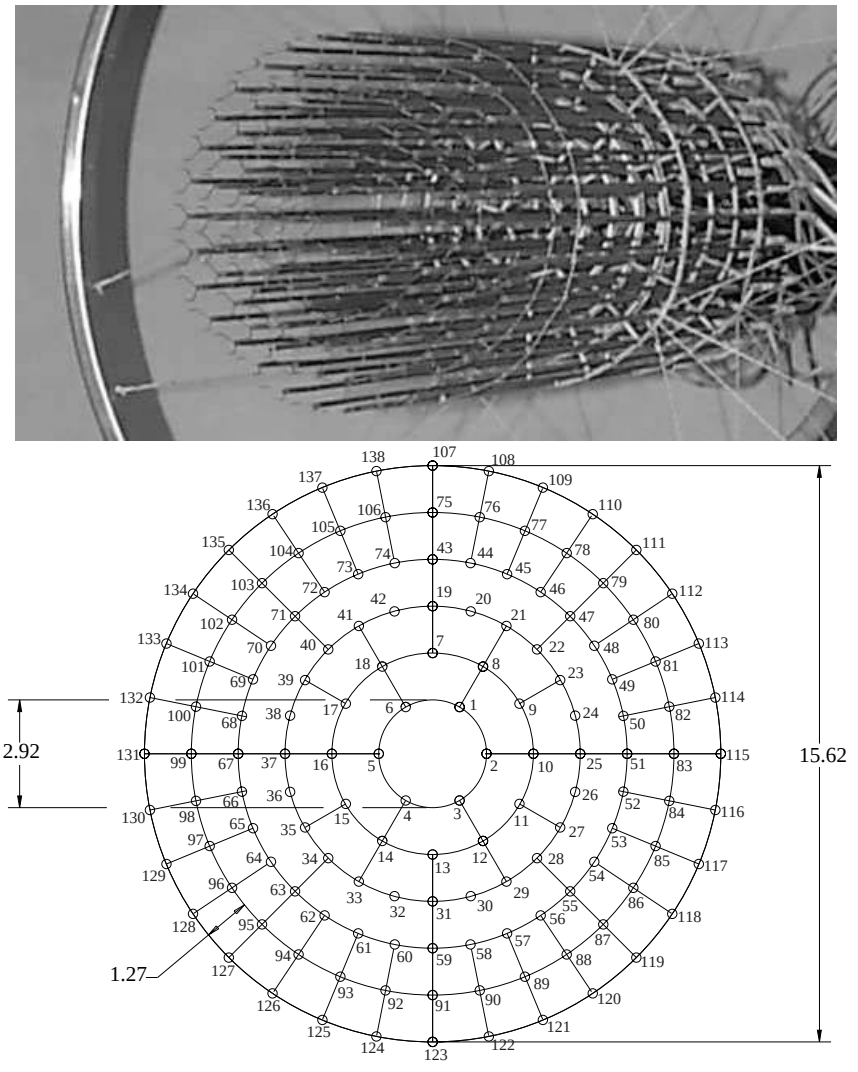

FIGURE 2. The 138 hot-wire probe array. Dimensions in cm.

they are sampled, a significant portion of the energy contained in scales smaller than the wires is not aliased into the lower modes. This procedure and analysis is described in detail in Citriniti & George (1997).

2.3. *Anemometers and sampling*

The long wires also acted as anti-aliasing filters in time with a nominal roll-off of approximately 1 kHz under the flow conditions. The sampling frequency of the signal was set up at 4 001.6 Hz, higher than the Nyquist criterion, ensuring no temporal aliasing. A confirming check by sampling at 142 kHz was done.

The anemometers were designed in the laboratory and optimized for this specific experiment. Their circuit performance and noise properties compared to industry standards (see Woodward, Ewing & Jernqvist 2001; Woodward 2001, for details). Data were acquired by a Microstar Laboratories DAP 5200a board which sampled simultaneously all 138 probes using a sample/hold amplifier, SHC298, in each

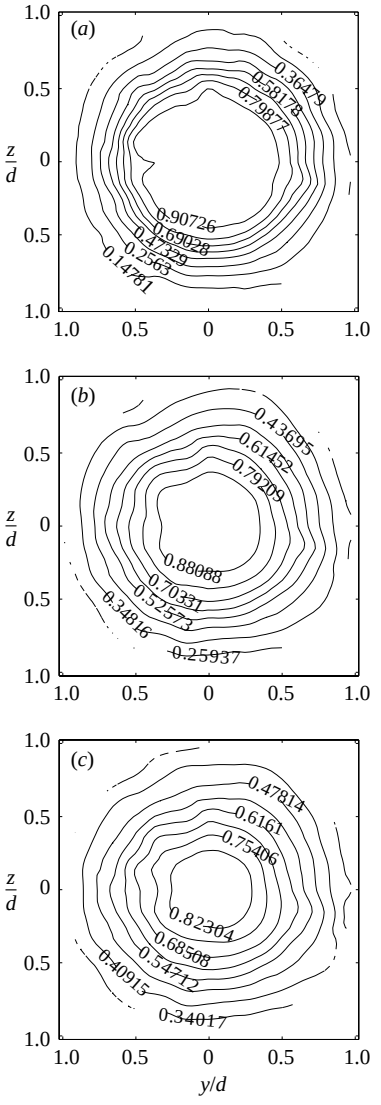

FIGURE 3. Mean velocity contours at $Re_D = 117\,600$ (exit velocity of 18 m s^{-1}), for different downstream positions: (*a*) $x/D = 2$, (*b*) 4, (*c*) 6.

anemometer board. Statistics were computed from 388 blocks of 4096 samples from each probe, corresponding to 400 s record length each, giving a variability of approximately 5% in the cross-spectral estimates.

3. Statistical properties

3.1. *Mean velocity profiles*

Contour maps of the mean velocity field normalized by the exit velocity for a Reynolds number of 117 600 are presented at three downstream positions in figure 3. They show that the mean velocity field is axisymmetric to within the statistical error, thus confirming that an axisymmetric shear layer has been formed. The plots also show that much of the velocity field is within the bounds of the probe array in the

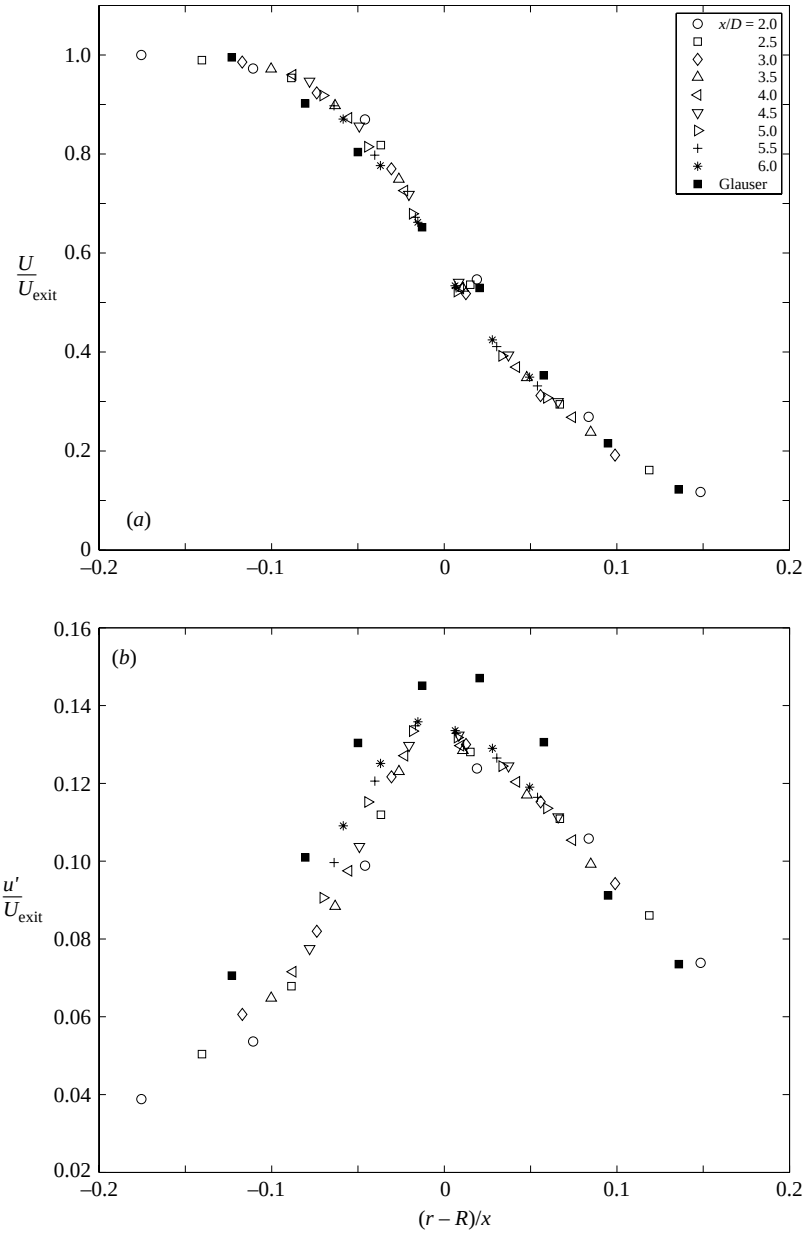

FIGURE 4. Normalized streamwise velocity along a radial line in the 138-wire probe array at $Re_D = 156\,800$. (*a*) Mean velocity. (*b*) Turbulence intensity. Also included are normalized profiles of Glauser (1987).

near jet, even for the $x/D = 6$ position where the outermost ring only extends to the position where the mean velocity is 36% of the centreline velocity.

Normalized mean streamwise velocity profiles are shown in figure 4(*a*) for the nine measured positions at the highest Reynolds numbers. The radial coordinate is normalized by the downstream distance, x, from the exit plane of the jet. These profiles were computed using probes 2, 5, 10, 16, 25, 37, 51, 67, 83, 99, 115, and 131 of the hot-wire probe array (see figure 2). The normalized mean velocity profile of

Glauser (1987), made in the same jet using 1 mm long, 5 μm wires, is also shown for comparison.

3.2. *Turbulence intensity profiles*

The turbulence intensity profiles shown in figure 4(*b*) collapse surprisingly well given that the filtering characteristics of the long wires change relative to the turbulence scales as the flow evolves downstream relative to the fixed array. The turbulence intensity based on the jet exit velocity is about 3% to 5% near the centreline of the jet, and the maximum turbulence intensity is about 13% to 14% at the peak near $(r-R)/x = 0$. The measurements are slightly lower than those of Glauser (1987), which were made in the same facility (at $Re_D = 110\,000$) with small hot wires. This is exactly as expected from the reduced temporal and spatial resolution of the long wires.

A note of caution is in order here: the long wires of the sensing element introduce deliberately both spatial and temporal filtering at the scales of the inertial subrange to remove small-scale energy for the purpose of minimizing aliasing in the spatial Fourier transforms reported herein. Therefore the turbulence intensities and one-dimensional spectra reported below are not suitable for use in overall energy balance considerations or turbulence model validation. This has been discussed in detail in Citriniti & George (1997), who show that the spatial filtering does not affect the large scales which are of primary interest to this work.

3.3. *Power spectral density*

The power spectra clearly vary greatly as a function of radial position, as shown in figure 5. On the higher speed side of the mixing layer, nearest the potential core, at $r/D = 0.15$, and 0.28, where the turbulence intensity is the lowest, local peaks are present corresponding to exit conditions. They disappear outside $r/D \geqslant 0.41$ as the turbulence intensity increases. On the lower speed side of the mixing layer, the spectra show at least one full decade of $f^{-5/3}$ range denoting high Reynolds number turbulent flow. Note that in this frequency range Taylor's frozen field hypothesis is applicable, so this corresponds to the $k^{-5/3}$ of the inertial subrange, see George, Beuther & Arndt (1984).

Citriniti & George (1997) showed that the long wires also affect the very low frequencies of the one-dimensional spectra because of the removal of small scales normally aliased into them. Nevertheless, the spectra are quite similar to these obtained by Petersen & Samet (1988), Glauser (1987), and Citriniti & George (2000).

4. Proper orthogonal decomposition

Mathematically, the proper orthogonal decomposition (POD) consists of projecting the random velocity field $u_i(\boldsymbol{x}, t)$ onto an orthonormal coordinate system $\phi_i(\boldsymbol{x}, t)$. The POD is a linear procedure, and produces a basis for the modal decomposition of an ensemble of functions, such as data obtained from experiments. It also provides the most efficient way of capturing the dominant components of an infinite-dimensional process with only a finite number of modes (Holmes *et al.* 1996; George 1988, 1999). The projection is optimal in the sense that the first projection captures most of the energy; or, mathematically speaking, the projection of the velocity field onto the function $\phi_i(\boldsymbol{x}, t)$ has to have maximal amplitude. The problem reduces to solving the integral equation:

$$\int_D R_{ij}(\boldsymbol{x}, t, \boldsymbol{x}', t')\,\phi_i(\boldsymbol{x}', t')\,\mathrm{d}(\boldsymbol{x}', t') = \lambda\,\phi_j(\boldsymbol{x}, t), \tag{4.1}$$

where $R_{ij} = \overline{u_i(\boldsymbol{x}, t) u_j^*(\boldsymbol{x}', t')}$ is the two-point cross-correlation tensor.

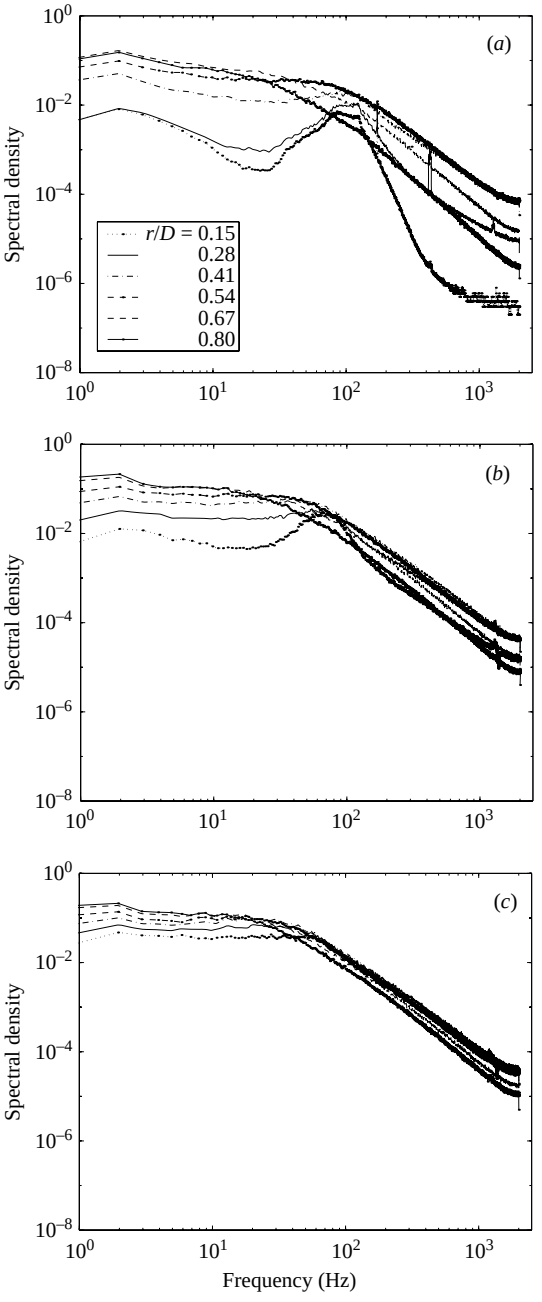

FIGURE 5. Power spectral densities along a radial line at $Re_D = 117\,600$ (exit velocity of 18 m s^{-1}), for different downstream positions: (*a*) $x/D = 2$, (*b*) 4, (*c*) 6.

The nature of the solutions to equation (4.1) depends on the domain of integration, D, and the properties of the field itself. If the field is of finite total energy and the kernel is Hermitian symmetric, then the solution can be found with Hilbert–Schmidt theory, and this is what is usually referred to as the POD. The axisymmetric jet flow field considered herein, however, is stationary in time, and homogeneous-periodic in the azimuthal direction. As a consequence, the eigenfunctions in these coordinates

can be easily proven to be the harmonic functions. Operationally, it is easiest to first Fourier transform the velocity field in these particular directions to obtain the doubly Fourier transformed field, $\hat{u}_i(x, r, m, f)$ (where m is the azimuthal mode number and f is the temporal frequency), then apply the Hilbert–Schmidt theory (or POD) to this transformed field (Citriniti & George 2000).

For the single velocity component considered here, the POD integral equation at each downstream position becomes

$$\int_D R_{x,x}(x; r, r', m, f)\phi_x^{(n)}(x, r', m, f)r' \,\mathrm{d}r' = \lambda^{(n)}(m, f; x)\phi_x^{(n)}(x, r, m, f) \tag{4.2}$$

where $R_{x,x}(x; r, r', m, f)$ is the two-point cross-spectral tensor of the streamwise velocity component, the $\lambda^{(n)}(m, f; x)$ are eigenvalues (or more properly eigenspectra) and the $\phi_x^{(n)}(x, r, m, f)$ are eigenfunctions for each POD mode, n, and are functions of azimuthal mode number, m, and frequency, f, with the latter also a function of radial direction, r. The superscript (n) anticipates that there is more than one solution as noted below. The r in the integral is the Jacobian for the cylindrical coordinate system, and D is in practice the radial extent for which the kernel is significantly different from zero. Since the POD is applied here only to measurements of the streamwise component at a given downstream position, x is only a parameter in the equations. This decomposition at downstream 'slices' across the flow is referred to as the 'slice-POD'. The relation of this single-component POD to the full tensorial version was considered in detail by Glauser (1987).

The Hilbert–Schmidt theory applied to equation (4.2) then yields the following:

(i) There exists not one but an infinity of solutions, but they are denumerable, i.e. $n = 1, 2, \ldots$. In practice the number available in an experiment is limited to the number of radial points for which the kernel is measured.

(ii) The eigenfunctions are orthonormal and therefore form a complete set for this space, i.e.

$$\int_D \phi_x^{(n)}(x, r, m, f)\, \phi_x^{(p)*}(x, r, m, f)\, r \,\mathrm{d}r = \delta_{np}, \tag{4.3}$$

where δ_{np} is the Kronecker delta function.

(iii) The eigenvalues (or eigenspectra), $\lambda^{(n)}(m, f; x)$ are ordered, i.e.

$$\lambda^{(1)} > \lambda^{(2)} > \lambda^{(3)} \cdots > 0, \tag{4.4}$$

and their sum over all POD modes (n), azimuthal modes (m) and integral over all frequencies (f) is equal to the resolved streamwise kinetic energy integrated over the cross-section:

$$E = \sum_n \sum_m \int_f \lambda^{(n)}(m, f; x)\,\mathrm{d}f. \tag{4.5}$$

(iv) The doubly Fourier transformed random velocity component, $\hat{u}_x(x, r, m, f)$, can be reconstructed from the eigenfunctions, i.e.

$$\hat{u}_x(x, r, m, f) = \sum_{n=1}^{\infty} a_n(m, f; x)\phi_x^{(n)}(x, r, m, f) \tag{4.6}$$

where the random coefficients for each POD mode are functions of m and f and given by

$$a_n(m, f; x) = \int_D \hat{u}_x(x, r, m, f)\, \phi_x^{(n)*}(x, r, m, f)\, r \,\mathrm{d}r. \tag{4.7}$$

These are uncorrelated and related to the eigenvalues by

$$\overline{a_n(m,\, f\,;x)a_p^*(m',\, f';x)} = \lambda^{(n)}(m,\, f\,;x)\delta(f'-f)\delta_{np}\delta_{mm'}. \tag{4.8}$$

By inverse transformation it is thus possible to reconstruct, either as a whole or in part, the instantaneous streamwise velocity component as a function of space and time.

(v) Finally, the cross-spectral kernel, $R_{x,x}(x\,;r,r',m,\,f)$, can be expressed as a bilinear combination of the eigenfunctions, $\phi_x^{(n)}(x,r,m,\,f)$, with a diagonal decomposition of the two-point cross-spectrum, i.e.

$$R_{x,x}(x\,;r,r',m,\,f) = \sum_{n=1}^{\infty} \lambda^{(n)}(m,\, f\,;x)\phi_x^{(n)}(x,r,m,\,f)\,\phi_x^{(n)*}(x,r',m,\,f). \tag{4.9}$$

It should be noted that the actual implementation of the decomposition is slightly altered by the presence of the Jacobian, r, in equation (4.2). Indeed, it is more advantageous to have a Hermitian symmetric kernel (Baker 1977). It can be made so by separating r' into $r'^{1/2} \times r'^{1/2}$, multiplying the entire equation by $r^{1/2}$, and redefining the two-point cross-spectral tensor and orthogonal function as $r^{1/2}\,R_{x,x}(r,r',m,\,f\,;x)\,r'^{1/2}$ and $\phi_x(r,m,\,f\,;x)\,r^{1/2}$ respectively. This only makes the computation easier, and does not have any influence on the results.

Appendices A and B summarize the symmetry properties of the kernel $R_{x,x}$ for the axisymmetric jet considered here. The results can be briefly summarized as follows: the eigenspectra $\lambda^{(n)}(x,m,\,f)$ are the same in all four quadrants, i.e. quadrant II ($m>0,\ f<0$), quadrant III ($m<0,\ f<0$), and quadrant IV ($m<0,\ f>0$) are the same as for quadrant I ($m>0,\ f>0$). The eigenfunctions differ slightly in that in quadrants I and II they are the same while in I and III they are complex conjugates, as they are in quadrants II and IV. Because of this, only data for $m>0,\ f>0$ are presented below.

5. Eigenspectra for $n=1,\ \lambda^{(1)}(m,\,f\,;x)$

From equation (4.5), it is clear that the eigenspectra show directly how the streamwise component of the kinetic energy is distributed with POD mode number, n, azimuthal mode number, m, and frequency, f. For all the data sets, the first eigenspectrum, $\lambda^{(1)}(m,\,f\,;x)$, integrated over frequency and summed over azimuthal modes accounts for 64.0% to 68.7% of the resolved streamwise energy.† Table 1 summarizes these results for the first three POD modes ($n=$ 1, 2, 3). Adding the first three POD modes provides more than 90% of the resolved portion of the kinetic energy of the flow. This agrees well with Citriniti & George (2000) and the earlier observations of Glauser & George (1987), both of whom found the first POD mode to dominate the decomposition.

Since only the streamwise component of the velocity was measured, the data have been normalized with the total resolved streamwise kinetic energy, or $\overline{u_x^2}$. Results are indeed quite different if the data are normalized by the total kinetic energy in the flow, $\overline{u_x^2}+\overline{u_r^2}+\overline{u_\theta^2}$, or by the two components measured by cross-wires, $\overline{u_x^2}+\overline{u_r^2}$, as in Glauser & George (1987) for example. For the jet mixing layer, $\overline{u_r^2} \approx \overline{u_\theta^2}$ (they

† Note that the 'resolved energy' is less than the actual energy in the flow because of the removal of small-scale energy by the long wires. Hence the percentages are higher than those based on fully resolved measurements, such as those reported by Glauser & George (1987).

Re_D	x/D	$\lambda^{(1)}$	$\lambda^{(1)}+\lambda^{(2)}$	$\lambda^{(1)}+\lambda^{(2)}+\lambda^{(3)}$
	2	66.79	84.91	94.78
	3	65.55	82.99	92.80
78 400	4	68.73	86.04	93.86
	5	67.98	85.62	93.64
	6	65.72	83.38	92.25
	2	66.13	85.21	95.15
	3	64.80	82.78	92.97
117 600	4	64.30	82.09	91.90
	5	64.26	82.10	91.60
	6	65.32	83.03	92.07
	2	66.18	85.18	95.25
	3	64.43	82.41	92.74
156 800	4	63.79	81.68	91.60
	5	64.03	81.90	91.45
	6	65.08	82.90	91.95

TABLE 1. Percentage of the streamwise resolved energy per POD mode.

are exactly equal on the centreline, due to axisymmetry) and $\overline{u_x^2} \approx 2\overline{u_r^2}$ (as seen approximately in measurements of Bradshaw, Ferriss & Johnson 1964; Hussain & Clark 1981; Glauser 1987). Using these, the total energy at a cross-section can be related to that of just the streamwise component; the results confirm to within a few percent the agreement among the amount of energy resolved by the POD in the previous experiments of Glauser & George (1987), Ukeiley *et al.* (1999), Taylor *et al.* (2001), Citriniti & George (2000) and the present one.

Figure 6 presents the eigenspectra for the first POD mode as a function of frequency, f, and azimuthal mode number, m, at $Re_D = 117\,600$. Note that only a single quadrant is shown since the others can, at least for these experiments, be determined from it (see the Appendices). From these three-dimensional plots several trends are immediately obvious. At $x/D = 2.0$, azimuthal mode-0 is spread over a band of frequencies which ranges from about 0 to 150 Hz, but this energy in mode-0 moves to lower frequencies as x/D increases. Corresponding to the diminution of mode-0 is the emergence of mode-1 and mode-2. In fact, the energy in the higher azimuthal modes peaks at about $m = 6$ at $x/D = 2$, and is concentrated at low frequencies (large streamwise spectral wavelengths)†, but clearly moves to lower azimuthal mode numbers as x/D increases.

6. Azimuthal dependence of the eigenspectra

The dependence of the eigenspectra on azimuthal mode number and downstream position alone is most easily seen using the normalized eigenvalue, $\xi^{(n)}(m;x)$, defined as

$$\xi^{(n)}(m;x) = \frac{\displaystyle\int_f \lambda^{(n)}(m,\, f;x)\,\mathrm{d}f}{\displaystyle\sum_n \sum_m \int_f \lambda^{(n)}(m,\, f;x)\,\mathrm{d}f}. \tag{6.1}$$

† Note that Taylor's frozen field hypothesis definitely does not apply at the lowest frequencies, but neither are they purely temporal, so their interpretation is ambiguous.

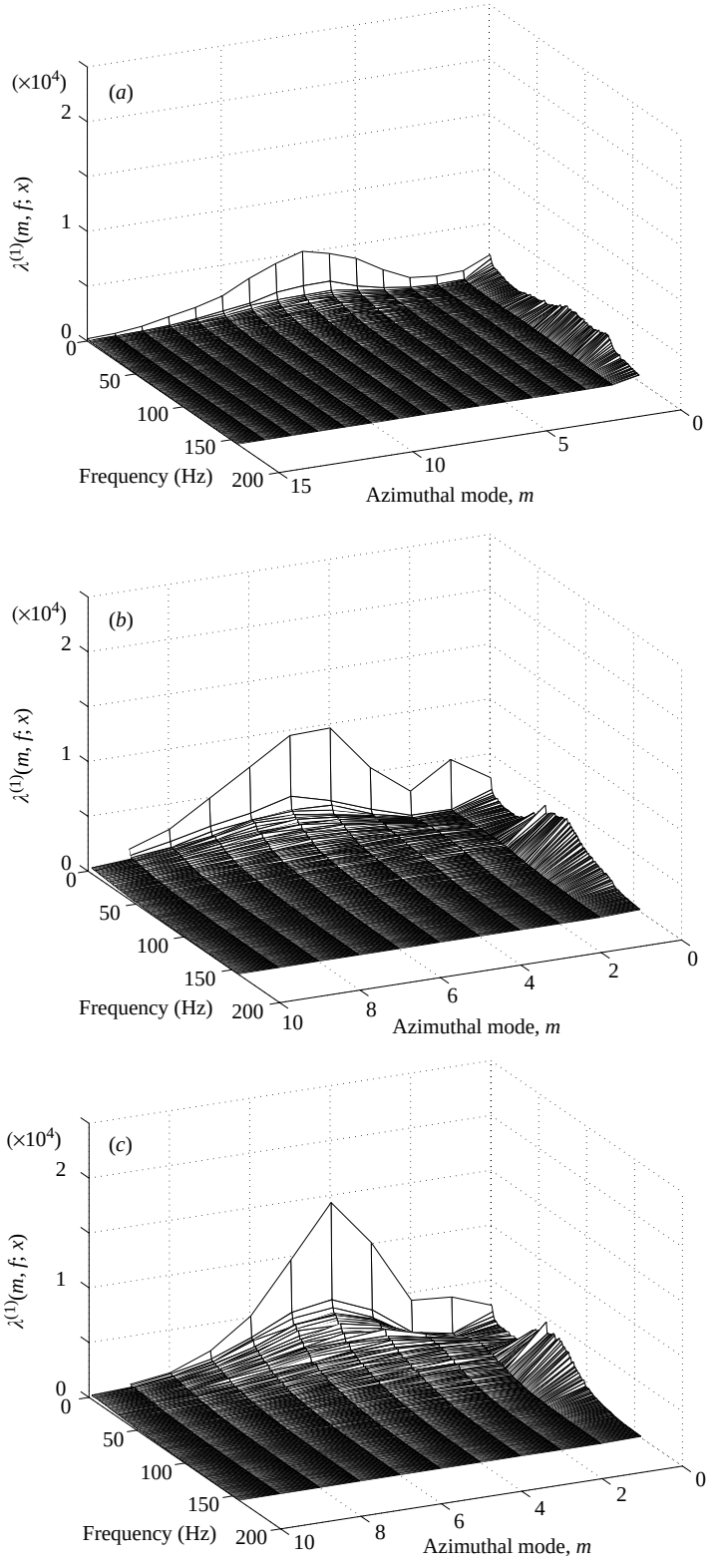

FIGURE 6(*a–c*). For caption see facing page.

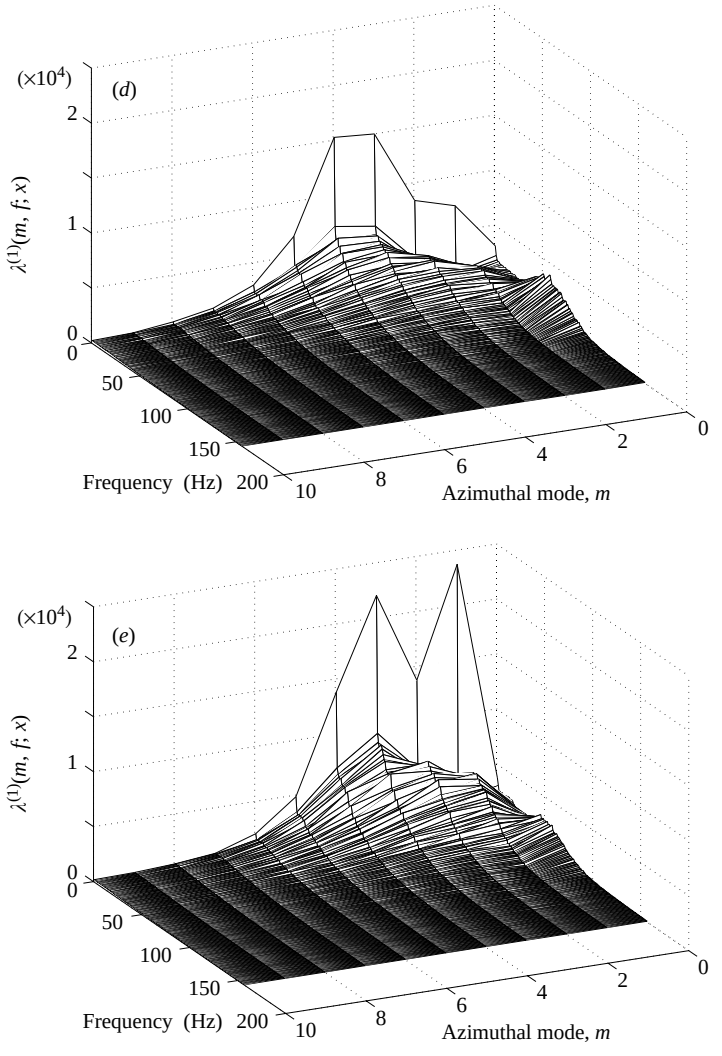

FIGURE 6. Eigenspectra for the first POD mode, $\lambda^{(1)}(m, f; x)$, as a function of azimuthal mode number, m, and frequency, f, for $Re_D = 117\,500$, at different downstream positions: (*a*) $x/D = 2$, (*b*) 3, (*c*) 4, (*d*) 5, (*e*) 6.

The denominator is the total resolved streamwise turbulent kinetic energy in the flow (see equation (4.5)). The numerator, on the other hand, is only integrated over frequency.

The azimuthal dependence of the normalized energy distributions of the first POD mode is presented in figure 7. As shown previously in figure 6, the azimuthal energy distribution of the eigenspectra has a strong dependence on downstream position. Azimuthal mode-0, $\xi^{(1)}(0; x)$, shown in figure 8 behaves in a manner entirely different than the higher azimuthal modes. The zeroth azimuthal-mode, which dominated the dynamics at $x/D = 3$ in the Glauser (1987) and Citriniti & George (2000) experiments, dies off rapidly downstream for all Reynolds numbers to a non-zero value that still exists in the far jet (see figure 8 and Part 2). It is clear that the dominant part of azimuthal mode-0 is a transient, and therefore events associated with it in the mixing layer are not likely to characterize the turbulence in the jet far

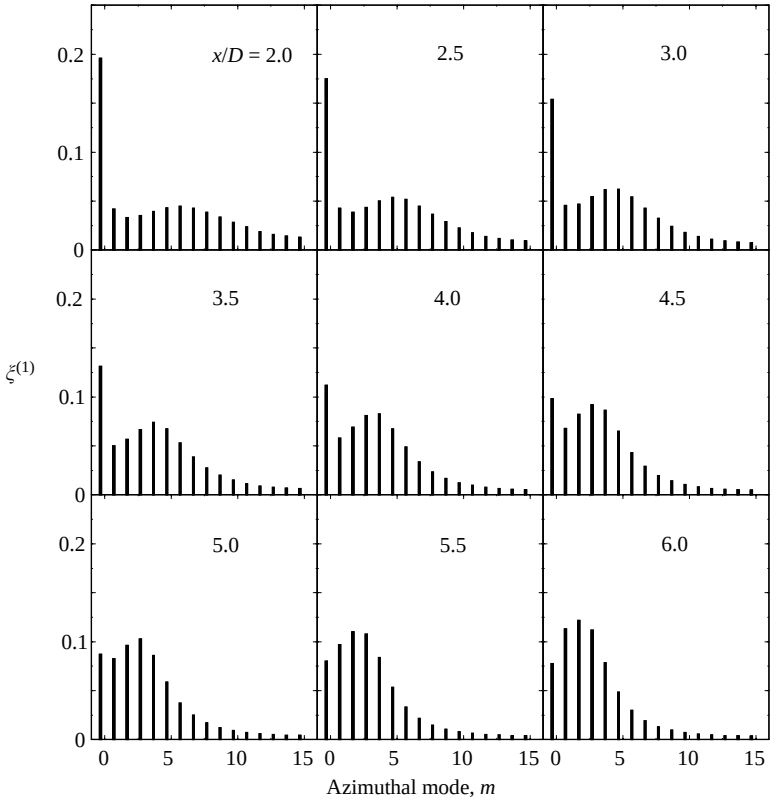

FIGURE 7. Normalized first POD mode energy distribution, $\xi^{(1)}(m;x)$, with azimuthal mode number, m, at $Re_D = 156\,800$.

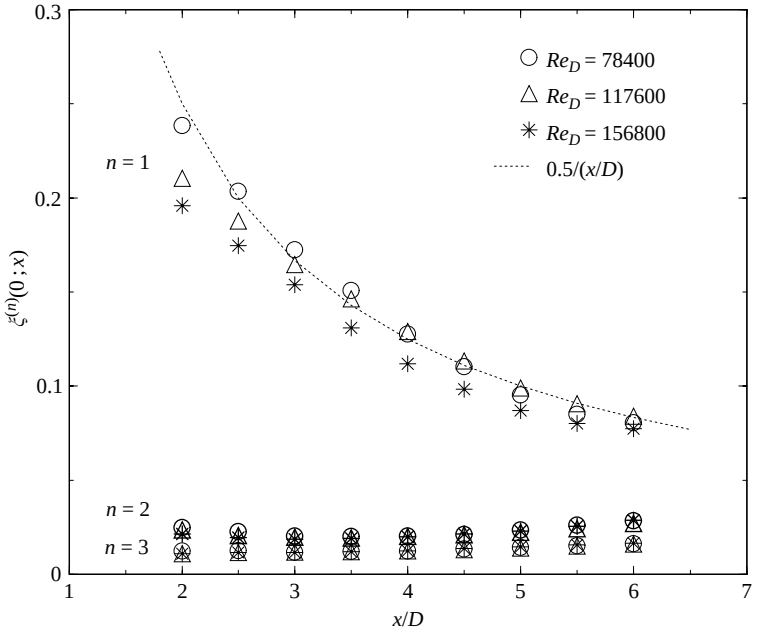

FIGURE 8. Variation with downstream position of the azimuthal mode-0 distribution for the first three POD modes $n =$ 1, 2, and 3 at $Re_D = 78\,400$, 117 600, and 156 800.

downstream, contrary to the suggestion of Citriniti & George (2000). Even so, since mode-0 would be zero if the flow were homogeneous in x, this suggests that the non-zero residual value may control (or be controlled by) the growth rate of the far jet.

For the higher azimuthal modes ($m \geqslant 1$), the peak shifts to lower mode numbers, while the amplitude actually increases with downstream distance. Note that similar results are seen for the second POD mode, $\xi^{(2)}(m;x)$. By $x/D = 6$, the peak is definitively at azimuthal mode-2, as first reported in Gamard *et al.* (2002). In Part 2 of this paper, it will be clear that there is no further evolution downstream even in the far jet.

Ukeiley & Seiner (1998) reported a similar evolution in a much higher Mach number axisymmetric jet. At Mach numbers of 0.3 and 0.6, the dominant azimuthal mode was $m = 3$ at 8 diameters downstream (Taylor *et al.* 2001). It seems likely that their higher dominant mode number is due to the fact that their measurements were still inside the potential core region, which ends farther downstream at their Mach numbers.

George *et al.* (1984) and Khwaja (1981) noted that the statistical properties of the axisymmetric jet shear layer appeared to scale in shear-layer similarity variables, even though the equations did not admit such solutions. Figure 9 shows the near collapse of the eigenvalues for the first two POD modes for $m \geqslant 1$ at all Reynolds numbers and positions, when normalized in shear-layer variables $\xi^{(n)}(m;x)/(x/D)$ vs. $m\ x/D$.

7. Frequency dependence of the eigenspectra

Experimentally, the frequency (or temporal variation) obtained by the measuring apparatus is a time variation of the signal seen by the device. Unfortunately its interpretation as space or time in the flow field is complicated by the fact the turbulence is being convected by the probes while it is also evolving in time. The so-called 'Taylor's frozen field hypothesis' assumes that convection dominates the evolution, so temporal variations can be interpreted as spatial variations. For a variety of reasons, Taylor's hypothesis should not be expected to be valid for the lowest frequencies in this flow, not the least of them being they would correspond to unphysical disturbances several metres long. Other reasons have been discussed in detail by Wills (1964) and Lumley (1965).

Figures 10 and 11 show the frequency content of the first POD eigenspectra for the first nine azimuthal modes at the Reynolds numbers of 117 600 and 156 800 respectively.

At $x/D = 2$, azimuthal mode-0 is dominant over all frequency ranges. By $x/D = 4$, azimuthal mode-0 has diminished enough so that it only dominates in a band around the Strouhal peak of the shear layer (between 0.35 and 0.5 depending on the Reynolds number). The spectra of the remaining modes have increased only slightly, and hardly change at all from $x/D = 4$ to 6. By contrast, azimuthal mode-0 continues to drop. By $x/D = 6$, only the lowest azimuthal modes dominate. This energy shift occurs mainly in the lower frequency range of $0 < f < 200$.

The local peak in the eigenspectra can be compared to the local peak of the velocity spectra taken from figure 5. The Strouhal numbers, $St_D = f D/U_{\text{exit}}$, based on the frequency of the local peak, f, the jet exit diameter, D, and the exit velocity, are plotted as a function of downstream position in figure 12. The Strouhal number peak is clearly associated with the azimuthal mode-0 behaviour, and its disappearance in

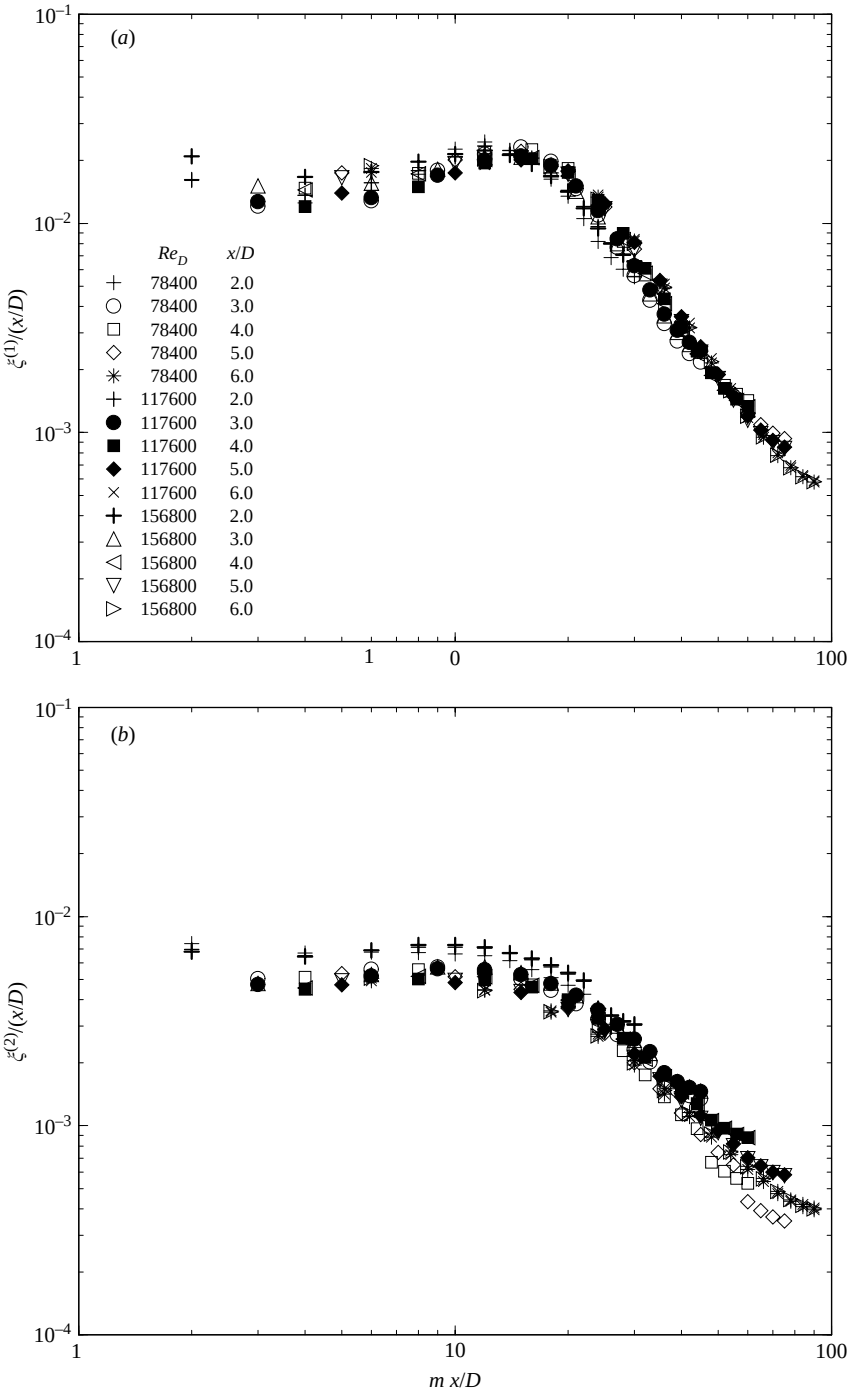

FIGURE 9. The first, (*a*), and second, (*b*), POD mode energy distribution for azimuthal mode $m \geqslant 1$ normalized in shear-layer variables, ($m\ x/D$), at $Re_D = 78\,400$, 117 600, and 156 800.

the velocity spectra by the end of the potential core is consistent with the decrease of azimuthal mode-0. The Strouhal numbers decrease with increasing downstream positions for the lower Reynolds numbers. By contrast, for the highest Reynolds

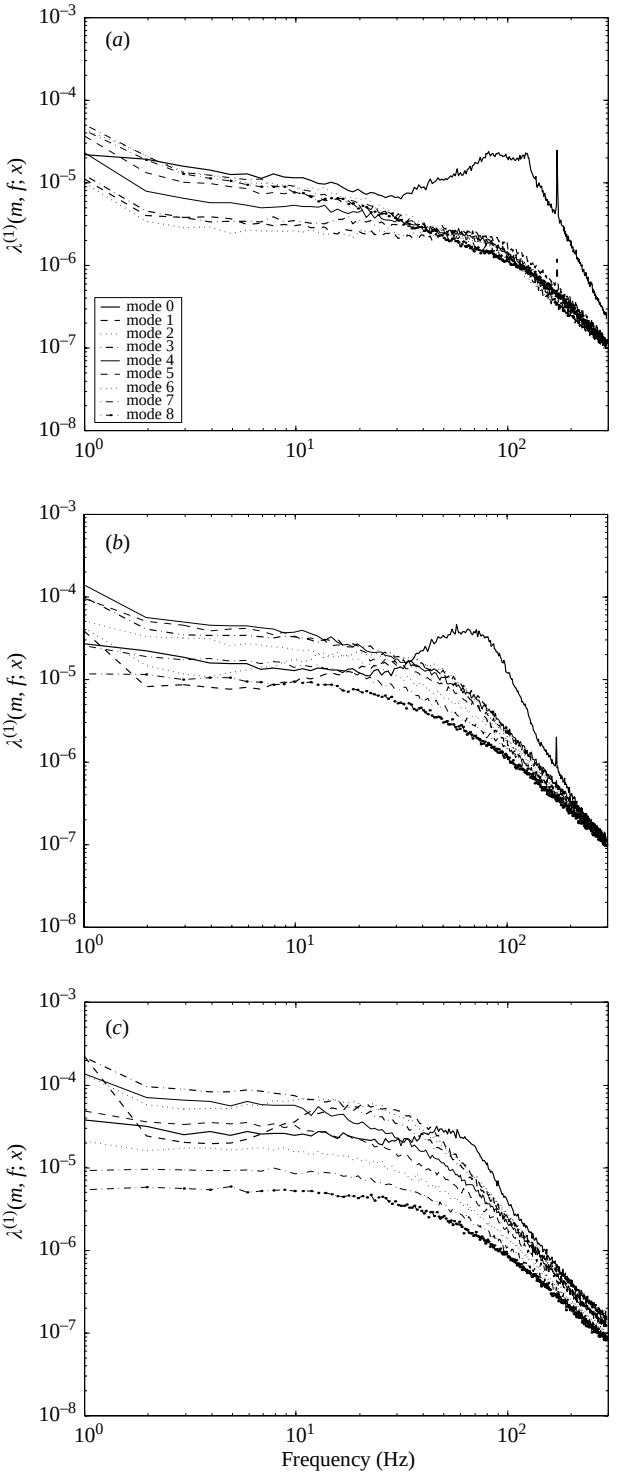

FIGURE 10. First POD mode eigenspectra at different azimuthal modes for $Re_D = 117\,600$. (*a*) $x/D = 2$, (*b*) 4, (*c*) 6.

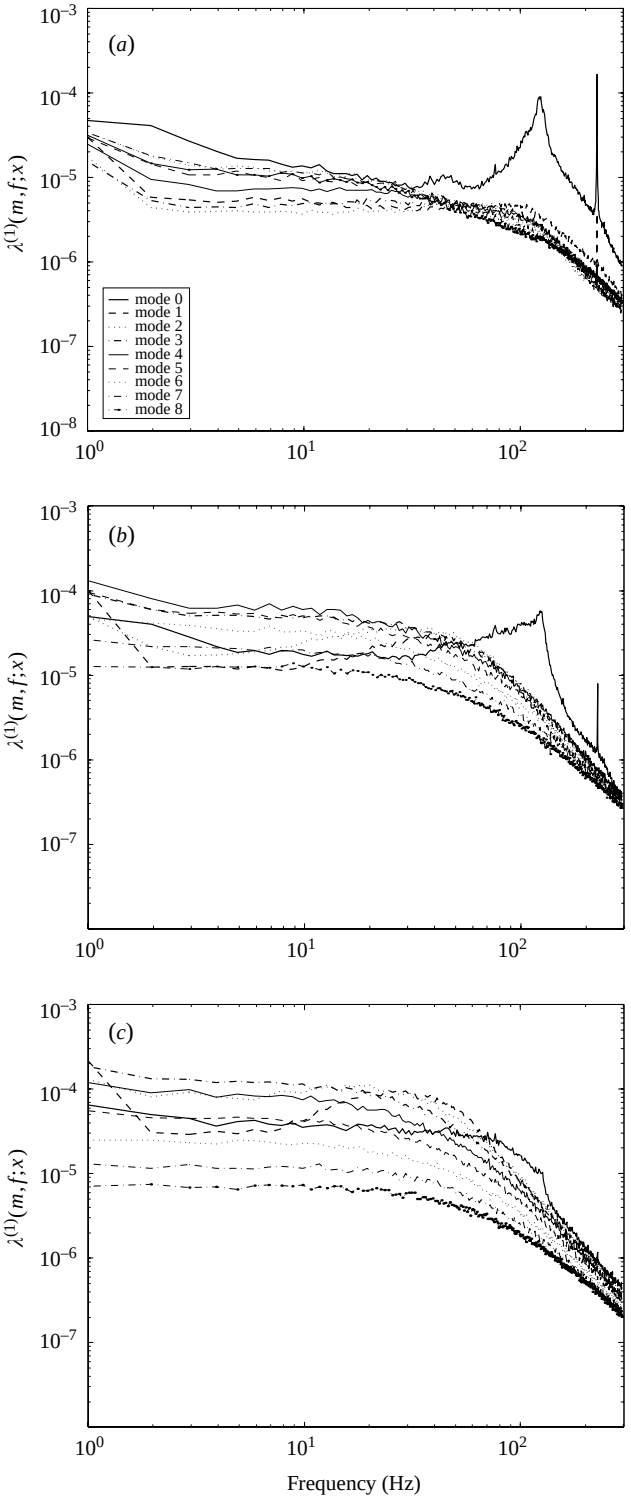

FIGURE 11. First POD mode eigenspectra at different azimuthal modes for $Re_D = 156\,800$. (*a*) $x/D = 2$, (*b*) 4, (*c*) 6.

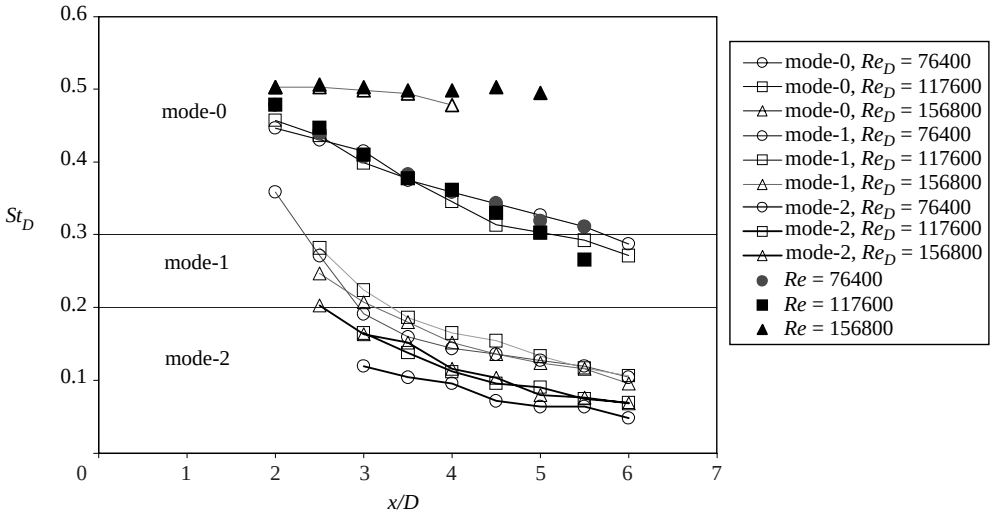

FIGURE 12. Strouhal numbers at various downstream locations for the three Reynolds numbers based on velocity spectra (filled symbols) and first POD eigenspectra (unfilled).

number, they are almost constant and independent of downstream position, consistent with the findings of Ho & Hsaio (1982).

8. The eigenfunctions

The eigenfunctions are functions of r, in addition to m, f, and x. Thus they contain the information about how the energy is distributed radially for the various modes. They can also be used to construct analytical models based on linear decompositions (see Ukeiley *et al.* 2001, for example).

Figure 13 presents slices of the normalized eigenfunctions for azimuthal mode-0 for the first POD mode at the frequency for which the corresponding eigenspectra peaks (different for each configuration). There is a radical change at approximately $x/D = 3$, after which all the real parts of the eigenfunctions exhibit the same behaviour.

The same slices, figure 14, show the eigenfunctions at the dominant azimuthal non-zero mode number for each downstream position, i.e. $m = 6$ at $x/D = 2$, $m = 5$ at $x/D = 3$, $m = 4$ at $x/D = 4$, $m = 3$ at $x/D = 5$, and $m = 2$ at $x/D = 6$. The eigenfunctions for azimuthal mode-0 resemble the linear spacewise stability eigenfunctions reported by Michalke (1964, 1965), consistent with the idea that azimuthal mode-0 is a convected disturbance. However, once the mean velocity profile loses its flat region, as in the farthest position at $x/D = 6$, the eigenfunctions are quite different. This will be shown in Part 2 to be in agreement with the fact that the eigenspectra have reached a 'far-jet' behaviour by this position, where azimuthal mode-1 is the convected instability, unlike the near-zero frequency peaks.

9. Reconstruction of the instantaneous velocity

To understand how the POD represents the original velocity signal, the instantaneous velocity field was reconstructed in the same manner as Citriniti & George (2000). These reconstructed fluctuating velocities illustrate how the dynamics and interactions of the large-scale structure change at different downstream positions for various Reynolds numbers.

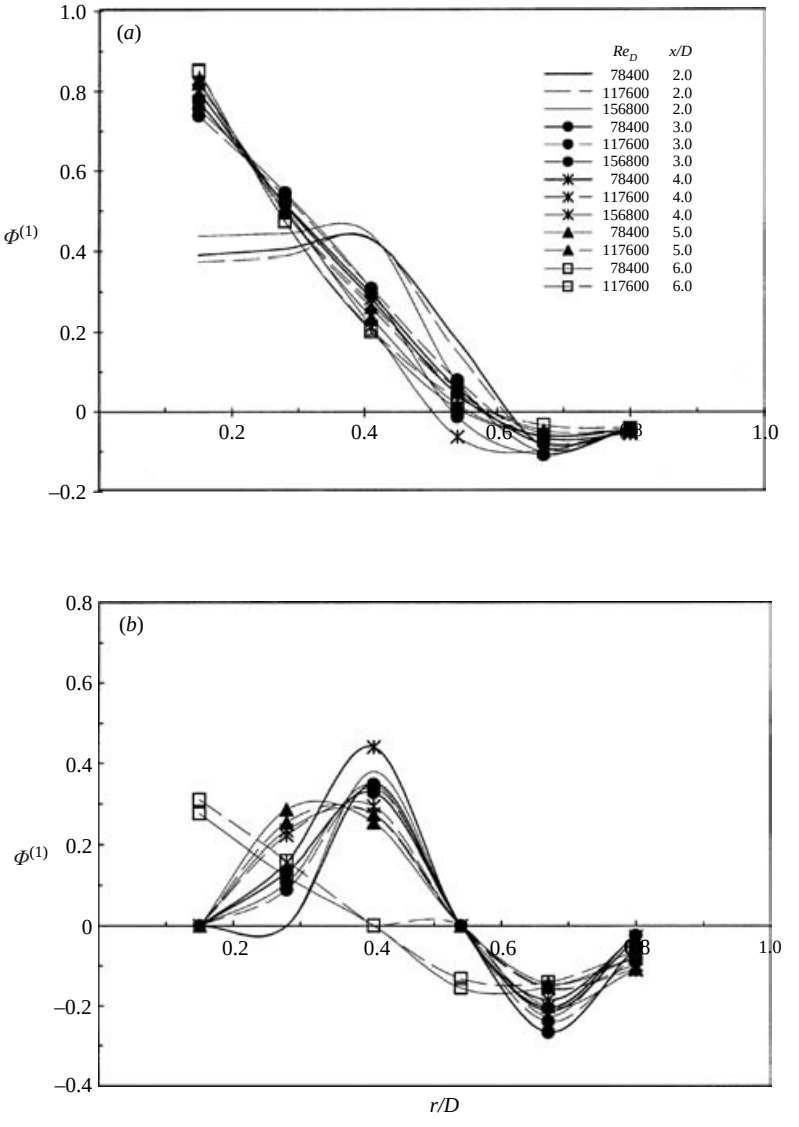

FIGURE 13. First eigenfunction (intensity multiplied by the jet diameter) for azimuthal mode-0 at three Reynolds numbers and five downstream positions. The frequency is the one corresponding to the peak in intensity of the spectrum at that downstream position. (*a*) Real part, (*b*) imaginary part.

Using the eigenvalue distribution, the velocity signal was reconstructed according to equations (4.6) and (4.7). Only the first POD mode ($n = 1$) was used for reconstruction since it dominated the turbulence kinetic energy. In order to clarify the role of the most energetic contributions to the flow, azimuthal mode numbers were chosen at each location using the results of figure 6 (see caption).

The data set for animation was chosen arbitrarily as the 234th block out of 388 blocks, starting at the 1 024th data sample in the block. Each time step or index has a real time span of 249.9 μs corresponding to the sampling frequency of 4 001.6 Hz.

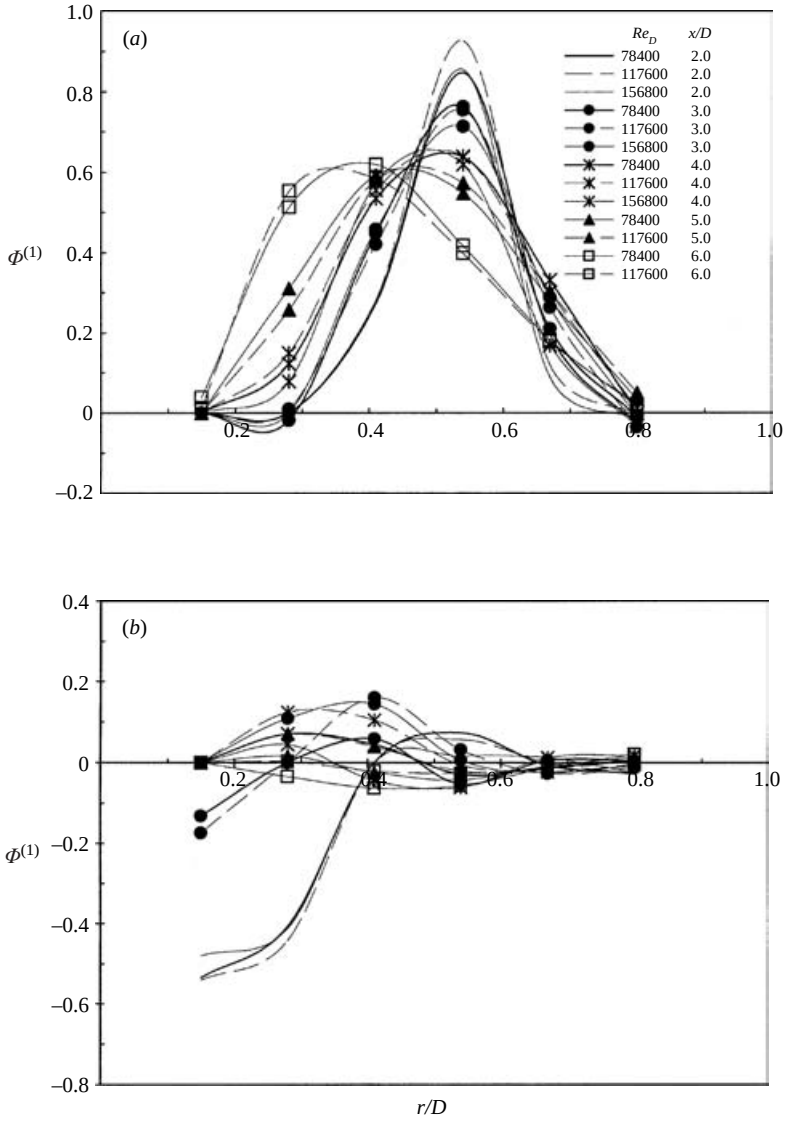

FIGURE 14. First eigenfunction (intensity multiplied by the jet diameter) for the most dominant non-zero azimuthal mode (at the considered downstream position) at three Reynolds numbers and five downstream positions. The frequency is the one corresponding to the peak in intensity of the spectrum at that downstream position. (*a*) Real part, (*b*) imaginary part.

Only a few frames are presented, which have been selected from the animated movies to describe the main characteristics of the coherent structures.

Figure 15 presents the main characteristics at $x/D = 2.0$. The azimuthally coherent 'volcano-like' eruption described by Citriniti & George (2000) is clearly present in figure 15(*a*), and it evolves in the same manner as they described. It was suggested by Citriniti & George (2000) that this was the result of the attempted leap-frogging of the azimuthally coherent vortex rings proposed by Grinstein, Glauser & George (1995). The eruption (figure 15*a*) forces high-velocity

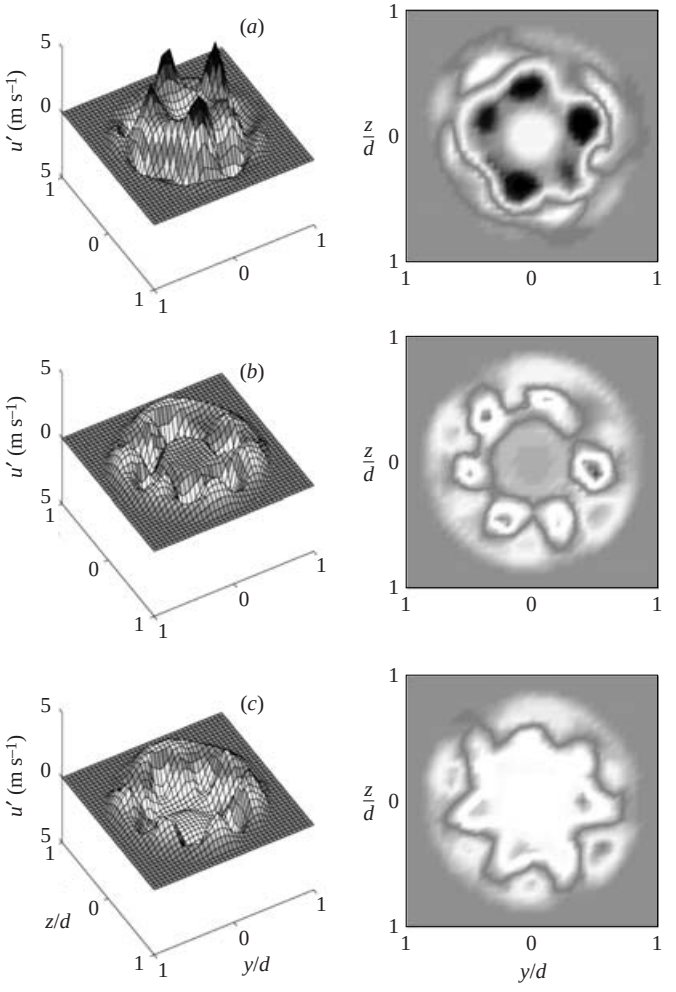

FIGURE 15. Reconstructed velocity field at $x/D = 2$ for $Re_D = 117\,600$ using only the first POD mode, and azimuthal mode numbers $m = 0$, 3, 4, 5, 6, 7. (*a*) $t_p = 1370$, (*b*) 1386, (*c*) 1394.

fluid through its centre along with the remnants of mode-6 in the potential core, while a new azimuthal mode-6 structure appears outside. The 'volcano' passes quickly leaving an azimuthally coherent structure (mode-6) in the potential core. Note that the higher modes (4 to 6) dominate the temporal pictures since they are mostly outside the core of the flow and are therefore swept past the probes more slowly. But it is the eruption that has most of the energy. The animation at higher Reynolds number shows the same evolution, but with more velocity fluctuation. The flow visualizations of Liepmann & Gharib (1992) showed coherent structures with similar characteristics in the potential core and outside region. They also showed streamwise vortex ribs around the volcano and azimuthal coherent structures in the braid region. This is consistent with the idea of the higher mode structure outside being entrained into a passing vortex ring.

While the mode-0 structure exists, the 'volcano-like' event shows a quasi-periodic behaviour in time. By counting the number of frames of the reconstructed velocity field, the passage frequency of a life-cycle of the mode-0 structure can be calculated

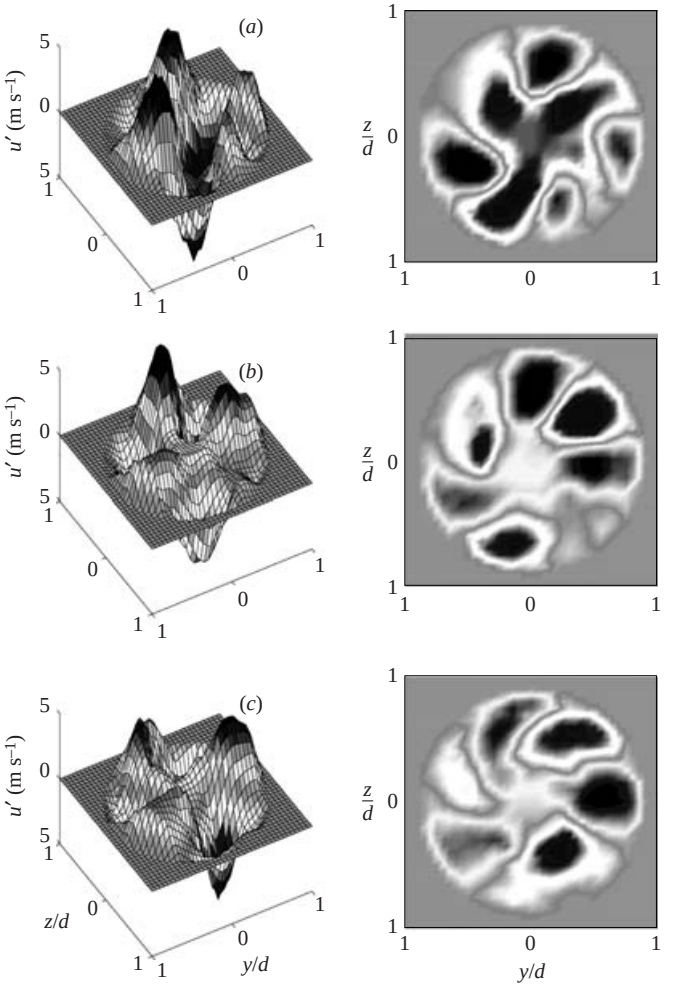

FIGURE 16. Reconstructed velocity field at $x/D = 4$ for $Re_D = 117\,600$ using only the first POD mode, and azimuthal mode numbers $m = 0$, 1, 2, 3, 4, 5. (*a*) $t_p = 1324$, (*b*) 1342, (*c*) 1370.

using the sampling frequency. The period of this 'volcano-like' event is the same as the Strouhal frequency peak of the velocity spectra (figure 12), which in turn corresponds to the frequency peak of the azimuthal mode-0 eigenspectra. Thus, it seems reasonable to conclude that all have a close relation to the 'volcano-like' eruptions which appear to dominate the dynamics at these upstream locations.

Unlike the reconstructions at $x/D = 2$ and 3, those at $x/D = 4$ are quite different, as shown in figure 16. The 'volcano-like' eruption still exists, but it is very weak. The most evident azimuthal mode changes from mode-4 to mode-3, consistent with the eigenspectra shown in figure 6.

At 5 diameters downstream for all Reynolds numbers, the features show disorganized evolution, and are not periodic. Mode-0 is very small and has almost disappeared. Unlike the volcano-like eruptions, a 'propeller-like' motion is observed, which rotates (or precesses) slowly from frame to frame. By $x/D = 6.0$, the structure is simpler. Mode-0 is almost gone, and only lower mode numbers are observed for all Reynolds numbers. Azimuthal mode-2 and mode-3 appear in figure 17, showing

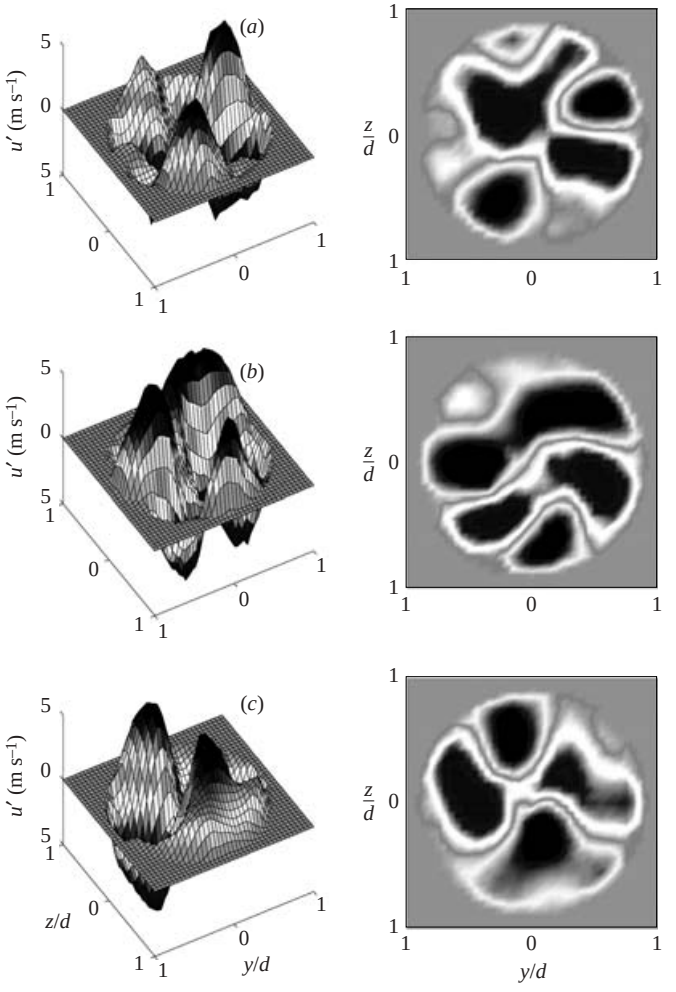

FIGURE 17. Reconstructed velocity field at $x/D = 6$ for $Re_D = 117\,600$ using only the first POD mode, and azimuthal mode numbers $m = 0$, 1, 2, 3, 4, 5. (*a*)$t_p = 1270$, (*b*) 1542, (*c*) 1620.

quite large-scale structure. Energy shifting from one peak to another is quite obvious. Various mode numbers are observed, but the lower mode numbers dominate the evolution.

It is clear that the coherent features of the flow change from 'volcano-like' eruptions to 'propeller-like' motion as the downstream distance is increased. This is consistent with the disappearance of azimuthal mode-0 from the eigenspectra (see figures 6 and 7) and the shift of the higher mode peak to lower mode numbers (from mode-6 at $x/D = 2.0$ to mode-2 at $x/D = 6.0$). Of course, over this same span the mean velocity profile has evolved from a near top-hat with a well-defined potential core to an almost fully developed jet profile.

10. Summary and conclusions

The large-scale structure of an axisymmetric mixing layer was investigated using a 138 hot-wire probe array for Reynolds numbers of 78 400, 117 600, and 156 800 from

$x/D = 2$ to 6. From application of the POD in the radial direction, it was observed that the first POD mode contains more than 60% of the resolved streamwise turbulent energy at all downstream positions and Reynolds numbers. The first two POD modes together contain more than 80%.

While the energy in azimuthal mode-0 moves to lower frequencies as x/D increases, its total energy decreases. Thus it appears that the dominance of azimuthal mode-0 in the initial near-field region of the jet characterizes a transient process. The higher modes have a totally different behaviour. For azimuthal mode greater than $m = 0$, the energy shifts from higher modes to lower modes as x/D increases, but remains at low frequencies. In fact, the eigenspectra collapse when scaled in shear-layer similarity variables, i.e. λ/xU_0^2 versus fx/U_0 and mx/D, exactly like the ordinary single-point spectra.

The eigenvalues have a strong dependence on the streamwise position, x/D. Their overall behaviour, however, bears a resemblance to those predicted from inviscid instability theory. In particular, Batchelor & Gill (1962) show that for a top-hat profile all modes are unstable, but mode-0 grows the fastest. Once the profile becomes fully developed, mode-0 is stable, and higher non-zero azimuthal modes grow the fastest. Similar conclusions were reached by Michalke (1984) as well, but for spatially growing disturbances. These linear stability results are very much like the behaviour of the most energetic POD modes, and even the eigenfunctions appear to be at least qualitatively similar.

The difference in frequency range between azimuthal mode-0 and the higher modes suggests that mode-0 is probably a spatially convected disturbance, a global mode that can be preferentially excited at the source, while the non-zero azimuthal modes might be local temporally growing disturbances. The completion of the evolution to azimuthal mode-2 dominance by $x/D = 6$ anticipates the evolution from a state dominated by the initial conditions to the final similarity state of the far jet (see Part 2 of this paper). This is consistent with the fact that the dominant Strouhal number of the velocity spectral peak in the mixing layer is seen to be closely related to the azimuthal mode-0 behaviour. When the Strouhal peak is not seen in the energy spectra any more, azimuthal mode-0 no longer dominates the energetics of the flow.

The energy distribution of the first POD mode has no dependence on Reynolds numbers over the range of these experiments. This is contrary to the suggestion of Holmes *et al.* (1996) that more complicated modal structures might evolve with increasing Reynolds number. On the other hand, this observation is consistent with the suggestion by Glauser (1987) and Citriniti & George (2000) (who based their arguments on the existence of a well-developed $k^{-5/3}$-range in their spectral data) that once the Reynolds number is sufficiently high, there should be no dependence.

The instantaneous fluctuating velocity field at each cross-section was reconstructed using the eigenfunctions and coefficients obtained from the projection onto the original instantaneous velocity measured by all of the probes (in the manner of Citriniti & George 2000). Near the jet exit, highly organized and near-periodic evolutions of the large-scale structures were observed. Azimuthally coherent vortex rings, the 'volcano-like' eruptions identified by Citriniti & George (2000), dominate the dynamics and the interactions of the structures until about $x/D \approx 4$. The passage frequency for the volcanic eruption reasonably matches the Strouhal frequency and the peak frequency of azimuthal mode-0 in the range of $x/D = 2$ to 4. Beyond $x/D \approx 4$, the 'volcano-like' eruptions die off rapidly, and a 'propeller-like' structure appears and dominates the pattern.

This work was initiated at the Turbulence Research Laboratory of the State University of New York at Buffalo, and continued with the move of TRL to the Chalmers University of Technology in Gothenburg, Sweden. It contains information from the dissertations of D. J. at the University at Buffalo, and of S. G. at Chalmers. The support of the US Air Force Office of Scientific Research under grant number F49620-98-1-0143, the National Science Foundation under grant CTS-9102863, the Korean Air Force Academy under grant KAFA02-1-4-20, and the Swedish Research Council under grant 2001-2641 are gratefully acknowledged. The authors would also like to thank S. H. Woodward for his valuable technical guidance and assistance during the experiments; and as well, P. B. V. Johansson and E. Eljack of Chalmers who played crucial roles in verifying experimentally the appropriate symmetry conditions. We are also grateful to a reviewer for raising an interesting question related to the symmetries which stimulated the Appendices.

Appendix A. Symmetry considerations for statistically axisymmetric flows without swirl

The non-swirling axisymmetric jet and the axisymmetric mixing layer from which it evolves can be shown by experiment to satisfy to an excellent approximation the following conditions: (i) homogeneous and periodic in the azimuthal direction, θ; and (ii) stationary in time, t. In symbols these imply that the two-point, two-time correlations of the velocity vector at a single downstream position, x, are given by

$$\langle u_i(x, r, \theta, t)u_j(x, r', \theta + \vartheta, t + \tau)\rangle = f_{i,j}(x, r, r'; \vartheta, \tau), \tag{A 1}$$

and are a function only of x, the two radial positions, r and r', the azimuthal separation, ϑ, and the time delay, τ. Corresponding to the experiments of this paper, only the streamwise component of the velocity at single downstream position will be considered, so the subscripts will be dropped. More complicated relations apply in general to the vector relations, and the conclusions below must be modified accordingly.

Correlations

Because the correlations must be independent of origin in θ or t, they are invariant to shifts of the origins by the amounts ϑ or τ respectively. Therefore the following must also be true:

$$\langle u(x, r, \theta, t)u(x, r', \theta + \vartheta, t + \tau)\rangle = \langle u(x, r, \theta - \vartheta, t)u(x, r', \theta, t + \tau)\rangle \tag{A 2}$$

$$= \langle u(x, r, \theta - \vartheta, t - \tau)u(x, r', \theta, t)\rangle \tag{A 3}$$

$$= \langle u(x, r, \theta, t - \tau)u(x, r', \theta + \vartheta, t)\rangle. \tag{A 4}$$

Note that it is in general not true, at least without additional assumptions, that $\langle u(x, r, \theta, t)u(x, r', \theta + \vartheta, t + \tau)\rangle = \langle u(x, r, \theta, t)u(x, r', \theta - \vartheta, t + \tau)\rangle$ or $\langle u(x, r, \theta, t)u(x, r', \theta + \vartheta, t + \tau)\rangle = \langle u(x, r, \theta, t)u(x, r', \theta + \vartheta, t - \tau)\rangle$; i.e, $f(x, r, r', \vartheta, \tau) \neq f(x, r, r', \vartheta, -\tau)$ and $f(x, r, r', \vartheta, \tau) \neq f(x, r, r', -\vartheta, \tau)$. This can be contrasted with the symmetries of the single-time two-point correlations or two-time single-point correlations which are symmetrical, e.g. if $r = r'$, then $f(x, r, r, \vartheta, 0) = f(x, r, r, -\vartheta, 0)$ and $f(x, r, r, 0, \tau) = f(x, r, r, 0, -\tau)$.

Two-point cross-spectra

Now consider the two-point cross-spectrum defined by

$$R_{x,x}(x, r, r'; m, f) \equiv \frac{1}{2\pi} \int_{-\pi}^{\pi} \mathrm{d}\vartheta \int_{-\infty}^{\infty} \mathrm{d}\tau \; \mathrm{e}^{-\mathrm{i}m\vartheta - \mathrm{i}2\pi f\tau} \langle u(x, r, \theta, t) u(x, r', \theta + \vartheta, t + \tau) \rangle. \tag{A 5}$$

From the perspective of this paper, the question that needs to be answered is: what is the relation of $R_{x,x}(x, r, r', m, f)$ to $R_{x,x}(x, r, r', m, -f)$, $R_{x,x}(x, r, r', -m, f)$, and $R_{x,x}(x, r, r', -m, -f)$? Or more simply, do both negative and positive values of m and f contain independent information, or is all the information contained in just the positive values? Since the cross-spectra form the kernel of the POD, clearly the question is of considerable importance.

First consider $R_{x,x}(x, r, r', -m, -f)$ given by

$$\begin{aligned} R_{x,x}(x, r, r'; -m, -f) &= \frac{1}{2\pi} \int_{-\pi}^{\pi} \mathrm{d}\vartheta \int_{-\infty}^{\infty} \mathrm{d}\tau \; \mathrm{e}^{+\mathrm{i}m\vartheta + \mathrm{i}2\pi f\tau} \langle u(x, r, \theta, t) u(x, r', \theta + \vartheta, t + \tau) \rangle \\ &= \frac{1}{2\pi} \int_{-\pi}^{\pi} \mathrm{d}\vartheta \int_{-\infty}^{\infty} \mathrm{d}\tau \; \mathrm{e}^{-\mathrm{i}m\vartheta - \mathrm{i}2\pi f\tau} \langle u(x, r, \theta, t) u(x, r', \theta - \vartheta, t - \tau) \rangle \\ &= \frac{1}{2\pi} \int_{-\pi}^{\pi} \mathrm{d}\vartheta \int_{-\infty}^{\infty} \mathrm{d}\tau \; \mathrm{e}^{-\mathrm{i}m\vartheta - \mathrm{i}2\pi f\tau} \langle u(x, r, \theta + \vartheta, t + \tau) u(x, r', \theta, t) \rangle \end{aligned} \tag{A 6}$$

where the second integral results from the transformations, $\vartheta \to -\vartheta$ and $\tau \to -\tau$, and the last from stationarity in time and homogeneity in θ. It follows then from the definition of $R_{x,x}$ that

$$R_{x,x}(x, r, r'; -m, -f) = R_{x,x}(x, r', r; m, f). \tag{A 7}$$

Alternatively, since the cross-correlation itself is real, it also follows immediately from the definition of equation (A 5) that

$$R_{x,x}(x, r, r'; -m, -f) = R^{*}_{x,x}(x, r, r'; m, f). \tag{A 8}$$

Thus the values of $R_{x,x}$ in the third quadrant ($m < 0$, $f < 0$) can be found from those in the first by simply interchanging r and r' of the cross-spectrum for positive values, or by taking the complex conjugate. But how about quadrants two and four, $m > 0$, $f < 0$ and $m < 0$, $f > 0$ respectively?

From the definition of (A 5) it follows that

$$\begin{aligned} R_{x,x}(x, r, r'; -m, f) &= \frac{1}{2\pi} \int_{-\pi}^{\pi} \mathrm{d}\vartheta \int_{-\infty}^{\infty} \mathrm{d}\tau \; \mathrm{e}^{+\mathrm{i}m\vartheta - \mathrm{i}2\pi f\tau} \langle u(x, r, \theta, t) u(x, r', \theta + \vartheta, t + \tau) \rangle \\ &= \frac{1}{2\pi} \int_{-\pi}^{\pi} \mathrm{d}\vartheta \int_{-\infty}^{\infty} \mathrm{d}\tau \; \mathrm{e}^{-\mathrm{i}m\vartheta - \mathrm{i}2\pi f\tau} \langle u(x, r, \theta, t) u(x, r', \theta - \vartheta, t + \tau) \rangle \end{aligned} \tag{A 9}$$

where the last step follows from the change of variables $\vartheta \to -\vartheta$.

Now interchange r and r' and consider

$$R_{x,x}(x,r',r;m,f) = \frac{1}{2\pi}\int_{-\pi}^{\pi} \mathrm{d}\vartheta \int_{-\infty}^{\infty} \mathrm{d}\tau\, \mathrm{e}^{-\mathrm{i}m\vartheta - \mathrm{i}2\pi f\tau} \langle u(x,r',\theta,t)u(x,r,\theta+\vartheta,t+\tau)\rangle$$
$$= \frac{1}{2\pi}\int_{-\pi}^{\pi} \mathrm{d}\vartheta \int_{-\infty}^{\infty} \mathrm{d}\tau\, \mathrm{e}^{-\mathrm{i}m\vartheta - \mathrm{i}2\pi f\tau} \langle u(x,r,\theta,t+\tau)u(x,r',\theta-\vartheta,t)\rangle \tag{A 10}$$

where the last step follows from homogeneity in θ.

It follows from this that

$$R_{x,x}(x,r',r;m,-f) = \frac{1}{2\pi}\int_{-\pi}^{\pi} \mathrm{d}\vartheta \int_{-\infty}^{\infty} \mathrm{d}\tau\, \mathrm{e}^{-\mathrm{i}m\vartheta + \mathrm{i}2\pi f\tau} \langle u(x,r,\theta,t+\tau)u(x,r',\theta-\vartheta,t)\rangle$$
$$= \frac{1}{2\pi}\int_{-\pi}^{\pi} \mathrm{d}\vartheta \int_{-\infty}^{\infty} \mathrm{d}\tau\, \mathrm{e}^{-\mathrm{i}m\vartheta - \mathrm{i}2\pi f\tau} \langle u(x,r,\theta,t-\tau)u(x,r',\theta-\vartheta,t)\rangle$$
$$= \frac{1}{2\pi}\int_{-\pi}^{\pi} \mathrm{d}\vartheta \int_{-\infty}^{\infty} \mathrm{d}\tau\, \mathrm{e}^{-\mathrm{i}m\vartheta - \mathrm{i}2\pi f\tau} \langle u(x,r,\theta,t)u(x,r',\theta-\vartheta,t+\tau)\rangle \tag{A 11}$$

where the second integral is achieved by transforming $\tau \to -\tau$, and the last step follows from stationarity in time.

But the last two integrals in equations (A 9) and (A 11) above are equal; therefore

$$R_{x,x}(x,r,r',-m,f) = R_{x,x}(x,r',r,m,-f). \tag{A 12}$$

It also follows immediately from the definitions as before that

$$R_{x,x}(x,r,r',-m,f) = R^{*}_{x,x}(x,r,r',m,-f). \tag{A 13}$$

Clearly both these indicate that if the cross-spectrum is known for $m<0, f>0$ then the values of $m>0, f<0$ can be obtained by either interchanging r and r' or by taking the complex conjugate, or vice versa.

In summary, stationarity in t and homogeneity in the azimuthal direction θ imply that the doubly transformed cross-spectra in quadrants I ($m>0, f>0$) and III ($m<0, f<0$) are related, and that quadrants II ($m>0, f<0$) and IV ($m<0, f>0$) are related. Unfortunately this seems to be as far as stationarity in t and homogeneity in θ lead: there is in general no relation between quadrants I and II (or IV). Thus, in the absence of additional information or constraints, the cross-spectrum $R_{x,x}(x,r,r',m,f)$ must be specified in at least two quadrants of m and f. An example of such an additional constraint is given in Appendix B.

Eigenspectra and eigenfunctions

Consider the eigenvalue problem posed by

$$\int_D R_{x,x}(x;r,r',-m,-f)\phi_x^{(n)}(x,r',-m,-f)r'\,\mathrm{d}r' = \lambda^{(n)}(-m,-f;x)\phi_x^{(n)}(x,r,-m,-f). \tag{A 14}$$

But taking the complex conjugate of the entire equation and substituting equation (A 8) for the kernel leads to

$$\int_D R_{x,x}(x;r,r',m,f)\phi_x^{(n)*}(x,r',-m,-f)r'\,\mathrm{d}r' = \lambda^{(n)}(-m,-f;x)\phi_x^{(n)*}(x,r,-m,-f) \tag{A 15}$$

where λ is real. But the kernel is the same as the original eigenvalue problem of equation (4.2); therefore the solutions must be the same. It follows immediately that

$$\lambda^{(n)}(-m, -f; x) = \lambda^{(n)}(m, f; x), \tag{A 16}$$

$$\phi_x^{(n)}(x, r, -m, -f) = \phi_x^{(n)*}(x, r, m, f). \tag{A 17}$$

Thus quadrant III ($m < 0, f < 0$) can be obtained from quadrant I ($m > 0, f > 0$), and vice versa.

Similar considerations show that

$$\lambda^{(n)}(-m, f; x) = \lambda^{(n)}(m, -f; x), \tag{A 18}$$

$$\phi_x^{(n)}(x, r, -m, f) = \phi_x^{(n)*}(x, r, m, -f). \tag{A 19}$$

Therefore quadrant IV can be obtained from quadrant II, and vice versa. Unfortunately there is no general relation between I and II (or IV), at least in the absence of additional constraints.

Appendix B. Special symmetry established by experiment

For all of the experiments reported herein it was possible to establish from the measured cross-spectra that for $m > 0$, to within experimental error, the following additional symmetry condition applied:

$$R_{x,x}(x; r, r', m, -f) = R_{x,x}(x; r, r', m, f). \tag{B 1}$$

This relation does not apply to all statistically axisymmetric flows and applies only to the jet (and perhaps not even to all jets); for example it does not apply to the axisymmetric wake, which appears to satisfy a different condition (Johansson & George 2004). By contrast, equations (A 7), (A 8), (A 12) and (A 13) are general and also apply here for all values of m including $m = 0$.

When added to the constraints of Appendix A, it is easy using the same methodology to show that this supplies the missing condition to obtain the cross-spectra in quadrants II, III, and IV in terms of the information in quadrant I alone. For example, consider the eigenvalue problem posed by

$$\int_D R_{x,x}(x; r, r', m, -f)\phi_x^{(n)}(x, r', m, -f) r' \, \mathrm{d}r' = \lambda^{(n)}(m, -f; x)\phi_x^{(n)}(x, r, m, -f). \tag{B 2}$$

From equation (B 1) it follows immediately that the solutions to this equation must be the same as for the original problem posed by equation (4.2). Therefore the following must be true:

$$\lambda^{(n)}(m, -f; x) = \lambda^{(n)}(m, f; x), \tag{B 3}$$

$$\phi_x^{(n)}(x, r, m, -f) = \phi_x^{(n)}(x, r, m, f). \tag{B 4}$$

Thus the values in quadrant II ($m > 0, f < 0$) are the same as for quadrant I. It is easy using the results of Appendix A to show that the eigenspectra must be the same in all quadrants, while the eigenfunctions in quadrants III and IV are the complex conjugates of those in I and II respectively. Hence only quadrant I data are shown in the body of the paper.

Interestingly, it is also straightforward to show that equation (B 1) implies that the two-point correlation transformed over frequency only is not symmetrical in the

separation angle, ϑ, as commonly assumed. It can be reconstructed from the Fourier series representation of $R_{x,x}(x;r,r',\vartheta,f)$ as follows:

$$B_{x,x}(x;r,r',\vartheta,f) = \sum_{m=-\infty}^{\infty} \mathrm{e}^{+\mathrm{i}m\vartheta} R_{x,x}(x;r,r',m,f). \tag{B 5}$$

This can be rewritten as a sum over positive values of m only as

$$\begin{aligned} B_{x,x}(x,;r,r',\vartheta,f) &= R_{x,x}(x;r,r',0,f) \\ &\quad + \sum_{m=1}^{\infty} \{\mathrm{e}^{+\mathrm{i}m\vartheta} R_{x,x}(x;r,r',m,f) + \mathrm{e}^{-\mathrm{i}m\vartheta} R_{x,x}(x;r,r',-m,f)\}. \end{aligned} \tag{B 6}$$

From equations (A 13) and (B 1) it follows immediately that

$$\begin{aligned} B_{x,x}(x;r,r',\vartheta,f) &= R_{x,x}(x;r,r',0,f) \\ &\quad + \sum_{m=1}^{\infty} \{\mathrm{e}^{+\mathrm{i}m\vartheta} R_{x,x}(x;r,r',m,f) + \mathrm{e}^{-\mathrm{i}m\vartheta} R^{*}_{x,x}(x;r,r',m,-f)\} \\ &= R_{x,x}(x;r,r',0,f) + \sum_{m=1}^{\infty} \{\mathrm{e}^{+\mathrm{i}m\vartheta} R_{x,x}(x;r,r',m,f) \\ &\quad + \mathrm{e}^{-\mathrm{i}m\vartheta}\ R^{*}{}_{x,x}(x;r,r',m,f)\} \\ &= R_{x,x}(x;r,r',0,f) + \sum_{m=1}^{\infty} 2[\mathrm{Re}\{R_{x,x}(x;r,r',m,f)\} \cos m\vartheta \\ &\quad - \mathrm{Im}\{R_{x,x}(x;r,r',m,f)\} \sin m\vartheta]\,. \end{aligned} \tag{B 7}$$

Clearly, $B_{x,x}(x;r,r',\vartheta,f)$ is not an even function of ϑ, and therefore not symmetrical in ϑ.

In conclusion it should be noted that it is not clear at the time of writing why equation (B 1) is true. Therefore in the absence of a theoretical explanation it should be regarded as tentative. One rationalization may be that all probes see a disturbance at the same time, consistent with the fact that the frequency variations are primarily due to spatial disturbances being convected by the probes. But this leaves open the question about swirling disturbances, for which this could not be true. Or perhaps the net effect of such swirling disturbances is to cancel out on the average, since one sign of rotation is equally likely as the other. An important clue may lie in the fact that the axisymmetric wake appears to satisfy a different condition, suggesting that the unique character of each flow is at least reflected in this difference, if indeed not determined by it.

REFERENCES

Baker, C. T. H. 1977 *The Numerical Treatment of Integral Equations*. Clarendon.

Batchelor, G. K. & Gill, E. A. 1962 Analysis of the instability of axisymmetic jets. *J. Fluid Mech.* **14**, 529–551.

Bradshaw, P., Ferriss, D. H. & Johnson, R. F. 1964 Turbulence in the noise producing region of a circular jet. *J. Fluid Mech.* **19**, 591–625.

Cantwell, B. J. 1981 Organized motion in turbulent flows. *Annu. Rev. Fluid Mech.* **13**, 457–515.

Citriniti, J. H. & George, W. K. 1997 The reduction of spatial aliasing by long hot-wire anemometer probes. *Exps. Fluids* **23**(3), 217–224.

Citriniti, J. H. & George, W. K. 2000 Reconstruction of the global velocity field in the axisymmetric mixing layer utilizing the proper orthogonal decomposition. *J. Fluid Mech.* **418**, 137–166.

Delville, J., Ukeiley, L., Cordier, L., Bonnet, J.-P. & Glauser, M. N. 1999 Examination of large scale structures in a plane mixing layer. Part 1. *J. Fluid Mech.* **391**, 91–122.

Gamard, S. 2002 The axisymmetric jet. PhD thesis, Chalmers University of Technology, Gothenburg, Sweden.

Gamard, S., George, W. K., Jung, D. & Woodward, S. 2002 Application of a 'slice' POD to the far field of an axisymmetric turbulent jet. *Phys. Fluids* **14**, 2515–2522.

Gamard, S., Jung, D. & George, W. K. 2004 Downstream evolution of the most energetic modes in a turbulent axisymmetric jet at high Reynolds number. Part 2. The far-field region. *J. Fluid Mech.* **514**, 205–230.

George, W. K. 1988 Insight into the dynamics of coherent structures from a proper orthogonal decomposition. In *The Structure of Near Wall Turbulence, Proc. Symp. on Near Wall Turbulence, Dubrovnik, Yugoslavia* (ed. S. Kline), pp. 168–180. Hemisphere.

George, W. K. 1999 Some thoughts on similarity, the pod, and finite boundaries. In *Fundamental Problematic Issues in Turbulence* (ed. A. Gyr, W. Kinzelbach & A. Tsinober), pp. 117–128. Birkhauser.

George, W. K., Beuther, P. D. & Arndt, R. E. A. 1984 Pressure spectra in turbulent free shear flows. *J. Fluid Mech.* **148**, 155–191.

Glauser, M. N. 1987 Coherent structures in the axisymmetric turbulent jet mixing layer. PhD thesis, State University of New York at Buffalo.

Glauser, M. N. & George, W. K. 1987 Orthogonal decomposition of the axisymmetric jet mixing layer including azimuthal dependence. In *Advances in Turbulence* (ed. G. Comte-Bellot & J. Mathieu), pp. 357–366. Springer.

Glauser, M. N. & George, W. K. 1992 Application of multipoint measurements for flow characterization. *Expl Thermal Fluid Sci.* **5**, 617–632.

Glauser, M., Taylor, J., Ukeiley, L., George, W. & Citriniti, J. 2000 A low dimensional description of the axisymmetirc trubulent jet: an update. *ERCOFTAC Bull.* **46**, 53–61.

Gordeyev, S. & Thomas, F. 2000 Coherent structure in the turbulent planar jet. *J. Fluid Mech.* **414**, 145–194.

Grinstein, F. F., Glauser, M. N. & George, W. K. 1995 Vorticity in Jets. In *Fluid Vortices* (ed. S. I. Green), pp. 65–94. Kluwer.

Ho, C. M. & Hsaio, F. B. 1982 In *Proc. IUTAM Symp. on Structure of Complex Turbulence Shear Flows, Marseille, France*, pp. 121–136.

Holmes, P., Lumley, J. L. & Berkooz, G. 1996 *Turbulence, Coherent Structures, Symmetry and Dynamical Systems*. Cambridge University Press.

Hussain, A. K. M. F. 1983 Coherent structures - reality and myth. *Phys. Fluids* **26**, 2816.

Hussain, A. K. M. F. & Clark, A. R. 1981 On the coherent structure of the axisymmetric mixing layer: a flow-visualization study. *J. Fluid Mech.* **104**, 263–294.

Hussein, H. J., Capp, S. P., & George, W. K. 1994 Velocity measurements in a high-Reynolds-number, momentum-conserving, axisymmetric, turbulent jet. *J. Fluid Mech.* **258**, 31–75.

Johansson, P. B. V. & George, W. K. 2004 The evolution of the axisymmetric wake. Part 2: Slice pod. *J. Fluid Mech.* (submitted).

Jung, D. 2001 An investigation of the Reynolds-number dependence of the axisymmetric jet mixing layer using a 138 hot-wire probe and the POD. PhD thesis, State University of New York at Buffalo.

Khwaja, M. S. S. 1981 Investigation of the turbulent axisymmetric jet mixing layer. Master's thesis, State University of New York at Buffalo.

Leib, S. J., Glauser, M. N. & George, W. K. 1984 An application of Lumley's orthogonal decomposition to the axisymmetric turbulent jet mixing layer. In *Proc. 9th Rolla Symp. on Turbulence in Fluids* (ed. Patterson & Zakin). Univ. of Missouri-Rolla.

Liepmann, D. & Gharib, M. 1992 The role of streamwise vorticity in the near-field entrainment of round jets. *J. Fluid Mech.* **245**, 643–668.

Lumley, J. L. 1965 On the interpretation of time spectra in high intensity shear flows. *Phys. Fluids* **8**, 1056–1062.

Michalke, A. 1964 On the inviscid instability of the hyperbolic-tangent velocity profile. *J. Fluid Mech.* **19**, 543–556.

Michalke, A. 1965 On spatially growing disturbances in an inviscid shear layer. *J. Fluid Mech.* **23**, 521–544.

Michalke, A. 1984 Survey on jet instability theory. *Prog. Aerospace Sci.* **21**, 159–199.

Petersen, R. A. & Samet, M. M. 1988 On the preferred mode of jet instability. *J. Fluid Mech.* **194**, 153–173.

Taylor, J. F., Ukeiley, L. S. & Glauser, M. N. 2001 A low-dimensional description of the compressible axisymmetric shear layer. *AIAA Paper* 2001–0292.

Ukeiley, L., Cordier, L., Manceau, R., Delville, J., Glauser, M. & Bonnet, J.-P. 2001 Examination of the large-scale structure in a turbulent plane mixing layer. Part 2 Dynamical systems model. *J. Fluid Mech.* **441**, 67–108.

Ukeiley, L. & Seiner, J. 1998 Examination of large scale structures in a transonic jet mixing layer. *Proc. ASME Fluids Engineering Conf. ASME FEDSM* 98-5234.

Ukeiley, L. S., Seiner, J. M. & Ponton, M. K. 1999 Azimuthal structure of an axisymmetric jet mixing layer. In *Proc. 3rd ASME/JSME Joint Fluids Engineering Conf. ASME FEDSM* 99-7252.

Wills, J. A. B. 1964 On convection velocities in turbulent shear flows. *J. Fluid Mech.* **20**, 417–432.

Woodward, S. H. 2001 Progress toward a massively parallel thermal anemometry system. Master's thesis, State University of New York at Buffalo.

Woodward, S. H., Ewing, D. & Jernqvist, L. 2001 Anemometer system review. In *Proc. Sixth Annual ASME Symp. on Thermal Anemometry, June 8–10, 2001, Melbourne, Australia.*